Available online at www.sciencedirect.com
ScienceDirect
International Journal of Plasticity 23 (2007) 44–86
INTERNATIONAL JOURNAL OF Plasticity
www.elsevier.com/locate/ijplas

Hardening evolution of AZ31B Mg sheet

X.Y. Lou [a], M. Li [b,1], R.K. Boger [a], S.R. Agnew [c], R.H. Wagoner [a,*]

[a] *Department of Materials Science and Engineering, The Ohio State University, 477 Watts Hall, 2041 College Road, Columbus, OH 43210, USA*
[b] *Abaqus Central, Inc., 1440 Innovation Place, W. Lafayette, IN 47906-1000, USA*
[c] *Department of Materials Science and Engineering, University of Virginia, 116 Engineer's Way, P.O. Box 400745, Charlottesville, VA 22904, USA*

Received 23 October 2005; received in final revised form 30 January 2006
Available online 6 May 2006

Abstract

The monotonic and cyclic mechanical behavior of O-temper AZ31B Mg sheet was measured in large-strain tension/compression and simple shear. Metallography, acoustic emission (AE), and texture measurements revealed twinning during in-plane compression and untwinning upon subsequent tension, producing asymmetric yield and hardening evolution. A working model of deformation mechanisms consistent with the results and with the literature was constructed on the basis of predominantly basal slip for initial tension, twinning for initial compression, and untwinning for tension following compression. The activation stress for twinning is larger than that for untwinning, presumably because of the need for nucleation. Increased accumulated hardening increases the twin nucleation stress, but has little effect on the untwinning stress. Multiple-cycle deformation tends to saturate, with larger strain cycles saturating more slowly. A novel analysis based on saturated cycling was used to estimate the relative magnitude of hardening effects related to twinning. For a 4% strain range, the obstacle strength of twins to slip is 3 MPa, approximately 1/3 the magnitude of textural hardening caused by twin formation (10 MPa). The difference in activation stress of twinning versus untwinning (11 MPa) is of the same magnitude as textural hardening.

Keywords: Magnesium alloy; Tension/compression testing; Simple shear testing; Texture; Acoustic emission; Plastic deformation; Slip; Twinning; Untwinning

* Corresponding author. Tel.: +1 614 292 2079; fax: +1 614 292 6530.
E-mail address: wagoner.2@osu.edu (R.H. Wagoner).
[1] Formerly Graduate Research Associate, Dept. Materials Science and Engineering, The Ohio State University.

0749-6419/$ - see front matter
doi:10.1016/j.ijplas.2006.03.005

1. Introduction

With increasing demand for the application of light materials in the transportation industry, the plastic deformation behavior of magnesium alloys has been of recent interest. Compared with casting counterparts, wrought magnesium alloys have better mechanical properties, including tensile properties (Roberts, 1960; Bettles and Gibson, 2005) and fatigue resistance (Duygulu and Agnew, 2003). However, because of poor formability at room temperature, the large-scale utilization of sheet-formed magnesium alloys, for example AZ31B magnesium alloy sheet, has not developed.

The low formability at room temperature mainly arises from the limited number of slip systems in the hexagonal close packed (HCP) Mg alloys. The dominant slip system of magnesium AZ31B alloy at room temperature is slip in the close packed direction $\langle 11\bar{2}0\rangle$ or $\langle a\rangle$ on the basal (0001) plane (Roberts, 1960). The critical resolved shear stress (CRSS) of basal slip in pure magnesium is about 0.5 MPa (Burke and Hibbard, 1952; Kelly and Hosford, 1968; Kleiner and Uggowitzer, 2004). Other slip systems, such as non-basal slip of $\langle a\rangle$ on prismatic $\{10\bar{1}0\}$ planes (Ward Flynn et al., 1961), $\langle a\rangle$ on pyramidal $\{10\bar{1}1\}$ planes and $\langle c+a\rangle$ on pyramidal $\{11\bar{2}2\}$ planes (Obara et al., 1973; Agnew et al., 2001) were also observed in magnesium, although their critical resolved shear stresses are two orders higher than basal slip (Kelly and Hosford, 1968; Kleiner and Uggowitzer, 2004). According to the Von Mises criterion (Von Mises, 1928; Taylor, 1938), five independent slip systems are needed to accommodate the arbitrary homogeneous deformation of polycrystalline materials. (Fewer deformation systems can accommodate certain special strain paths.) Basal $\langle a\rangle$ slip, prismatic $\langle a\rangle$ slip and pyramidal $\langle a\rangle$ slip provide only four independent slip systems. Pyramidal $\langle c+a\rangle$ slip, which in principle provides the additional independent slip systems, is difficult to activate at room temperature because of its high CRSS (Agnew et al., 2001; Yoo et al., 2002). At elevated temperature, the activation of pyramidal $\langle c+a\rangle$ slip and other non-basal slip occurs at lower CRSS, reducing flow stress and increasing formability (Agnew and Duygulu, 2003, 2005). At room temperature, twinning can provide an independent deformation mechanism (in addition to basal and non-basal $\langle a\rangle$ slip systems) to satisfy the Von Mises criterion (Kocks and Westlake, 1967).

In HCP crystals, the twinning systems are strongly correlated with c/a ratio (Partridge, 1967; Yoo, 1981). The c/a ratio for pure magnesium is 1.624 (Roberts, 1960), which is close to, but less than, the ideal hard-sphere value of 1.633. Two common twin modes, $\{10\bar{1}2\}\langle 10\bar{1}\bar{1}\rangle$ and $\{10\bar{1}1\}\langle 10\bar{1}\bar{2}\rangle$, are observed in magnesium (Yoo, 1981), with $\{10\bar{1}2\}\langle 10\bar{1}\bar{1}\rangle$ being the most common and easily activated twin in magnesium and many other HCP metals (Roberts, 1960; Partridge, 1967; Kelly and Hosford, 1968). A CRSS for twinning, while low (Koike, 2005), is not well established because twin nucleation is inhomogeneous and depends on microstructure features (Partridge, 1967; Reed-Hill and Abbaschian, 1994). A fresh twin has a higher nucleation stress than the stress to propagate an existing twin (Partridge, 1965; Reed-Hill and Abbaschian, 1994).

Because of crystal symmetry, the shear direction for $\{10\bar{1}2\}$ twin reverses at $c/a=\sqrt{3}$. Since the c/a ratio of magnesium is smaller than $\sqrt{3}$, the $\{10\bar{1}2\}$ twin is a ‘tension’ twin, that is, its activation is associated with extension parallel to the c-axis in the HCP crystal structure (Yoo, 1981), and with contraction in a direction lying normal to $\langle c\rangle$. Because of the polar nature of twinning, the shear can occur only in one direction rather than opposite directions (Kocks and Westlake, 1967; Agnew and Duygulu, 2005). Therefore, a contraction along the c-axis cannot be accommodated by a $\{10\bar{1}2\}$ twin. In magnesium, a theoretical maximum extension of 6.4% along c-axis can be accommodated by complete reorientation of $\{10\bar{1}2\}\langle 10\bar{1}\bar{1}\rangle$ twins (Kocks and Westlake, 1967). After twinning, the c-axis will reorient to lie approximately in the original basal plane (Nave and Barnett, 2004).

Rolled AZ31B magnesium sheet alloy usually has very strong basal texture generated by rolling (Roberts, 1960; Agnew et al., 2001; Yukutake et al., 2003; Styczynski et al., 2004), where the c-axis of HCP lattice is predominantly aligned parallel to the sheet normal (McDonald, 1937; Yukutake et al., 2003). A state of stress which causes an extension in the sheet normal direction will activate twinning at low stress, while a state of stress that causes contraction normal to the sheet plane does not activate twinning (Kocks and Westlake, 1967; Reed-Hill, 1973; Gharghouri et al., 1999; Agnew et al., 2001; Nobre et al., 2002; Staroselsky and Anand, 2003; Styczynski et al., 2004). Conversely, an in-plane compression activates twinning but in-plane extension does not (Reed-Hill and Abbaschian, 1994). Of course, local inhomogeneities from grain-to-grain interactions can activate limited twinning, particularly in view of the limited number of independent slip systems, as can orientations of some grains that do not lie in the predominant basal texture.

Table 1 summarizes CRSS values reported for Mg and its alloys containing aluminum and zinc solutes. The upper section represents single-crystal data for Mg and dilute

Table 1
Critical resolved shear stresses (CRSS) reported for magnesium and its aluminum–zinc alloy

Metals	Conditions	$CRSS_{basal}$ (Mpa)	$CRSS_{twin}$ (Mpa)	$CRSS_{prism}$ (Mpa)	$CRSS_{twin}$/ $CRSS_{basal}$	$CRSS_{prism}$/ $CRSS_{basal}$
Mg	SC	0.81[a]; 0.76[b]; 0.45[c]; 0.65[d]; 0.52[e]	2[f]	39.2[g]	2.5 – 4.4	48 – 87
Mg 0.5 at. pct Zn	SC		2.7–2.8[h]			
AZ31B	PC, VPSC, XRD	45[i]	15[i]	110[i]	0.33[i]	2.4[i]
AZ31B	PC, EPSC, ND	10[j]	30[j]	55[j]	3[j]	5.5[j]
AZ31B	PC, Taylor, XRD				2[k]	1–2.4[k]
AZ31B	PC, TEM					1.1[l]
AZ31B	PC, ND, Schmid factor		25–35[m]			
AZ61	PC, XRD					1.5–2[n]
Mg 7.7 at. pct Al	PC, ND		65–75[o]			

SC, single crystal; PC, polycrystal; XRD, X-ray diffraction; ND, neutron diffraction; VPSC, visco-plastic self-consistent model; EPSC, elasto-plastic self-consistent model; Taylor, Taylor model.

[a] Schmid (1931).
[b] Bakarian and Mathewson (1943).
[c] Burke and Hibbard (1952).
[d] Hsu and Cullity (1954).
[e] Conrad and Robertson (1957).
[f] Reed-Hill and Robertson (1957a,b); Miura (2004).
[g] Reed-Hill and Robertson (1957a,b).
[h] Miura (2004).
[i] Agnew (2002).
[j] Agnew et al. (2003).
[k] Styczynski et al. (2004).
[l] Koike et al. (2003).
[m] Brown et al. (2005).
[n] Koike and Ohyama (2005).
[o] Gharghouri (1997).

Mg–Zn. Clearly, basal slip has the lowest CRSS, ranging from 0.45 to 0.81 MPa. Twinning has a CRSS two-to-four times larger, and prismatic slip has a CRSS much larger, 48–87 times.

There is apparently no single-crystal data for AZ31B (second section of Table 1). Instead, CRSS values are fit by polycrystal texture calculations in order to match the macroscopic response, or CRSS values are obtained using in situ neutron diffraction to track lattice strain and peak intensity variation (Gharghouri et al., 1999; Brown et al., 2005). The texture calculations include unknown errors and effects of stress concentration, grain size, and incompatibility. The scatter is quite large. The neutron diffraction results in yield activation stresses only for twinning. Nonetheless, some generalizations may be drawn. It appears that the addition of aluminum and zinc solutes raises the CRSS for all deformation mechanisms, as expected, and compresses the ratios among them. For example, the basal slip CRSS is in the range of 10–45 MPa while the CRSS range for twinning is 15–35 MPa. Thus, basal slip and twinning have roughly equal CRSS's, as compared with twinning having a CRSS twice that of basal slip in pure Mg. Prismatic slip in AZ31B has even more scattered results, with CRSS varying from 1-to-5 times that of basal slip, as compared with 48–87 times in pure Mg.

Sheet materials are typically formed by combinations of bending and stretching, both of which are dominated by in-plane loading, with much smaller through-thickness stresses. Therefore, the in-plane plastic deformation properties are of interest for sheet forming application. The yield stress for in-plane compression of Mg sheet is typically one half of that for in-plane tension (Ball and Prangnell, 1994; Nobre et al., 2002). After yield, the compressive hardening curve exhibits an inflected stress–strain curve with initially low strain hardening rate, distinct from the tensile behavior of AZ31B Mg alloy (Klimanek and Potzsch, 2002; Nobre et al., 2002; Yukutake et al., 2003; Barnett et al., 2004; Nave and Barnett, 2004). At larger compressive strain, when twinning is exhausted, or nearly so, and slip dominates, the compressive hardening curve takes on the appearance of the tensile one (Yukutake et al., 2003). At high temperatures, as twinning is suppressed by lower slip system CRSS's, the inflection hardening curve disappears (Yukutake et al., 2003).

In addition to dislocation slip and twinning, untwinning (or detwinning) may occur in a twinned material. It is responsible for the shape memory effect in shape memory alloys (Liu et al., 1999; Liu and Xie, 2003; Sehitoglu et al., 2003), where untwinning is the growth of one variant in martensite at the expense of another (Liu and Xie, 2003; Sehitoglu et al., 2003). Microscopically, untwinning can be characterized by the disappearance of existing twin bands. Deformed magnesium alloy, which has a high density of twins, can undergo untwinning (Caceres et al., 2003; Keshavarz and Barnett, 2005). Twins can disappear or become narrower under reverse loading or unloading, and can reappear under reloading. The crystal deformation process of untwinning is similar to twinning, although nucleation is not required or occurs more readily. Therefore, untwinning can also result in an inflected and concave strain hardening behavior (Kleiner and Uggowitzer, 2004). The strain caused by twinning in compression can be reversed by untwinning in subsequent tension. Untwinning is a contraction of twinned regions, a process that does not require nucleation (Partridge, 1965). The stress required for untwinning is less than that for twinning nucleation, but greater than that for twinning growth (Partridge, 1965). In cyclic loading, twinning and untwinning appear alternately (Gharghouri et al., 1999).

Understanding the large strain plastic behavior of sheet alloys along non-proportional strain paths is an important requirement for sheet metal forming application. The

Bauschinger Effect (Bauschinger, 1886), which refers to a lower yield stress developed with strain upon reverse loading following an initial strain/stress path, has been related to various mechanisms: residual stresses generated in forward deformation (Abel, 1987), Orowan loops around strong precipitates (Atkinson et al., 1974; Brown, 1977), internal stress from dislocation interactions (Hasegawa et al., 1986), and dislocation pileups at grain boundaries (Margolin et al., 1978). Regardless of mechanism, the macroscopic interpretation involves development of a "back stress" during loading that assists reverse loading.

The foregoing interpretations of the Bauschinger Effect rely on material hardening characteristics of dislocation slip. In materials that twin significantly, twinning and its interaction with slip can provide alternate Bauschinger Effect mechanisms. The twin boundaries operate as hard but deformable obstacles, with dislocation pileups developing at the twin boundaries which generate a long-range back stress field and large Bauschinger Effect (Karaman et al., 2001). In magnesium alloys at room temperature, where deformation in some stress states depends intimately on twinning, large asymmetry of cyclic deformation has been noted (Attari et al., 1990), but not studied in detail, particularly at large strain. Noster and Scholtes (2003) reported a pronounced Bauschinger Effect for small strain reversal. Consistent with the role of twins as obstacles for slip, pre-compression followed by tension was reported to produce a larger Bauschinger Effect than the opposite path, pre-tension followed by compression.

In contrast to extensive studies of magnesium bulk alloys, there is little data for large-strain in-plane compression of magnesium sheet alloys. Such measurements are limited by buckling. The large-strain cyclic deformation behavior of magnesium alloy, important to sheet metal forming behavior and simulation, has not been reported. Knowledge of the Bauschinger Effect, and more generally of the evolution of yield and hardening under non-proportional loading paths, is required to enable development of novel forming methods to take advantage of the unusual plastic properties of wrought Mg sheet.

In the current work, the constitutive behavior of O-tempered AZ31B Mg sheet alloy was investigated at room temperature. Monotonic and continuous reverse-path tests were conducted in uniaxial tension/compression and simple shear. Novel test designs were utilized to obtain large-strain deformation (Gsell et al., 1983; Rauch and Schmitt, 1989; Rauch, 1998; Balakrishnan, 1999; Lopes et al., 2003; Boger et al., 2005). In order to understand the origins of the mechanical response, optical metallography, texture analysis and acoustic emission measurements were conducted in parallel with the mechanical tests.

2. Experimental procedures

O-temper Mg AZ31B sheet alloy was mechanically tested at room temperature using novel tension/compression (Balakrishnan, 1999; Boger et al., 2005) and simple shear (Gsell et al., 1983; Rauch and Schmitt, 1989; Rauch, 1998; Lopes et al., 2003) tests. The deformation mechanisms were revealed by standard optical metallography, texture measurement, and acoustic emission.

2.1. Materials

AZ31B magnesium alloy sheet, which is a commercial alloy produced by Magnesium Elektron (Magnesium, 2005) and distributed by Mark Metals Inc. (MetalMart, 2005),

Table 2
Chemical compositions and elastic properties of AZ31B Mg alloy

Chemical composition (wt%)				Elastic properties (Cubberly et al., 1979)		
Mg	Al	Zn	Mn	Elastic modulus (GPa)	Shear modulus (GPa)	Poisson's ratio, ν
95.8	3.0	1.0	0.2	45	17	0.35

has chemical compositions and elastic properties as listed in Table 2. The additional aluminum and zinc act as solute atoms to strengthen magnesium alloy (Cubberly et al., 1979).

Three thicknesses and processing paths were tested. Sheet with 6.4 mm thickness was received in the O-condition. Sheet with 3.2 mm thickness was received in the H24 condition. Sheet with 1.0 mm thickness was processed by a high density infrared (Horton et al., 2005a) heating and rolling technique starting from O-temper 6.4 mm sheet at Oak Ridge National Laboratory. To eliminate the residual stresses from cutting and processing and to standardize the microstructures, all the materials were annealed at 345 °C for 2 h to obtain the O-temper (Cubberly et al., 1979; Agnew, 2003).

2.2. Uniaxial tensile tests

Standard ASTM tensile specimens (ASTM-E8-00, 2000) were machined parallel to the rolling direction (RD), transverse direction (TD), and 45° to the rolling directions (45°), with a rectangular cross-section of 13 mm width by 1, 3.2, or 6.4 mm thickness and a gage length of 50 mm. Testing was carried out using an Instron 1322 universal testing machine with a 245 kN load cell and an Electronic Instrument Research LE-05 laser extensometer.

Fig. 1 shows typical uniaxial tensile test results. As shown in Fig. 1a, in the normal tensile testing strain rate range of 10^{-4} to 10^{-3}/s, there is little effect of rate. The remainder of tests in the current work was carried out at a nominal initial strain rate of 1×10^{-3}/s at a constant crosshead speed. Fig. 1b shows that the sheets of three thicknesses have nearly identical mechanical properties. Note that the abrupt fracture behavior is quite different from ductile failure by plastic strain localization for low-strength sheet alloys with cubic crystal structures. Fig. 2 illustrates the brittle nature of fracture for AZ31B (left specimen), which occurs with little evidence of plastic localization (necking) in either the width or thickness directions. In contrast, the tensile fracture of aluminum alloy 6013, peak aged (right specimen), shows significant plastic localization in both directions before a shear-type failure occurs.

The tensile Lankford coefficient (r-value, defined as the plastic width strain divided by the plastic thickness strain in tension) was measured by interrupting tensile tests at known axial extension and measuring the corresponding specimen width. Because the thickness change was small and thus involved large relative measurement uncertainty, the measured axial strain (ε_l) and width strain (ε_w) were used with assumed volume constancy to infer the thickness strain (ε_t). In contrast, because the width change in compression was small compared with the thickness change, the compressive r-value was measured by stopping compressive tests at known axial compressive strains and measuring the corresponding specimen thickness. The tensile and compressive r-values are computed as follows:

$$r_{\text{tensile}} \equiv \frac{\Delta\varepsilon_w^p}{\Delta\varepsilon_t^p} = -\frac{\Delta\varepsilon_w^p}{\Delta\varepsilon_w^p + \Delta\varepsilon_l^p}, \quad r_{\text{compressive}} \equiv \frac{\Delta\varepsilon_w^p}{\Delta\varepsilon_t^p} = -\frac{\Delta\varepsilon_t^p + \Delta\varepsilon_l^p}{\Delta\varepsilon_t^p} \tag{1}$$

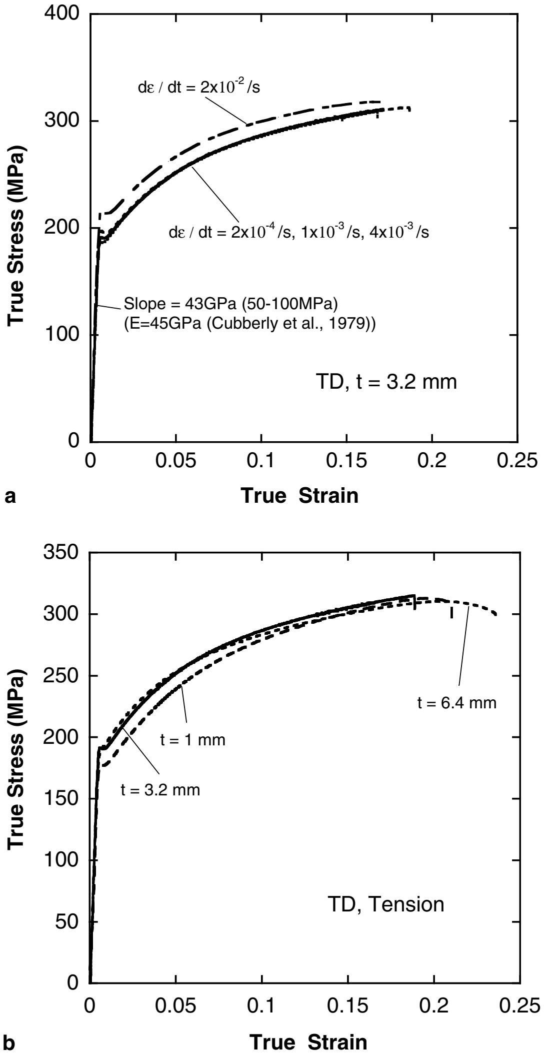

Fig. 1. Baseline tensile hardening. (a) Effect of strain rate; (b) comparison of three material thicknesses.

where p refers to plastic strain, and l, w and t refer to length, width and thickness, respectively. For cumulative *r*-values, as commonly reported, the changes of strain are taken from the beginning of the tests. For instantaneous *r*-values, of more relevance to plastic yield function forms, the strain increments are computed in the vicinity of the current strain.

The plastic strains were obtained from the total strains by subtracting elastic strains, as follows:

$$\varepsilon_{\mathrm{l}}^{\mathrm{p}} = \varepsilon_{\mathrm{l}} - \frac{\sigma_{\mathrm{l}}}{E} \tag{2}$$

$$\varepsilon_{\mathrm{w}}^{\mathrm{p}} = \varepsilon_{\mathrm{w}} + \nu \frac{\sigma_{\mathrm{l}}}{E} \tag{3}$$

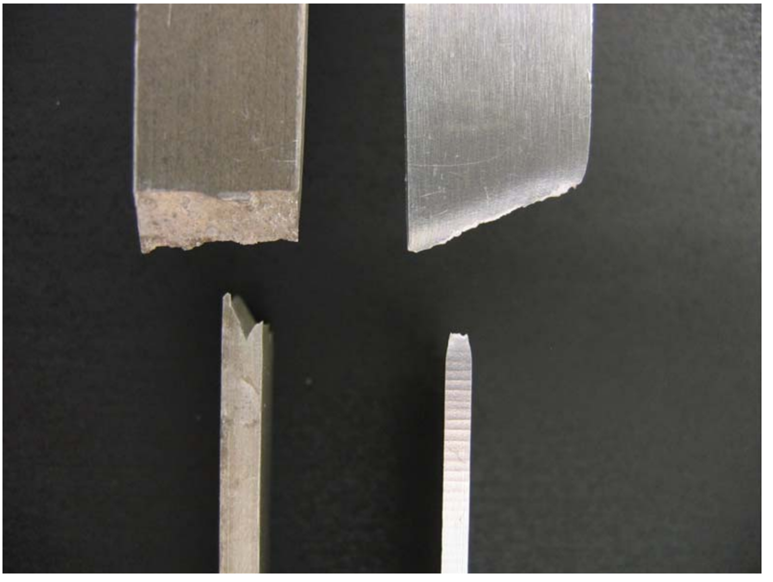

Fig. 2. Tensile fracture characteristics of AZ31B (left) and aluminum alloy 6013, peak-aged.

where E is Young's modulus (Table 2) and ν is Poisson's ratio (Table 2), and σ_1 is the longitudinal stress.

2.3. Compression and cyclic tests

Large compressive strains, which are critical for many sheet metal forming operations, cannot be obtained easily in the planes of the sheet materials because of the limitation of buckling. A test method developed by Boger et al. (2005), which relies on through-thickness sheet stabilization to avoid buckling, was used to extend the attainable strain range of Mg sheet in compression to approximately -0.08. A schematic of the novel tension/compression test (Boger et al., 2005) and the sample dimensions are shown in Fig. 3. Two flat steel plates and a hydraulic cylinder system were used to provide side force to support the exaggerated dog-bone specimen. Side forces of 12 kN were used to stabilize the sheet sample. A laser extensometer (Boger et al., 2005) was used to measure specimen extension directly.

The cyclic loading test was carried out using 3.2 and 6.4 mm thick samples. All mechanical tests were carried out under displacement control, except the multiple-cycle tests which were performed under strain control to improve the precision of the strain limits for each cycle. The experiments were repeated to establish reproducibility; the standard deviation for compression was found to be ± 6 MPa.

The stabilizing side force requires correction for two effects in order to obtain uniaxial stress–strain curves comparable to standard tensile testing: (1) friction between the sample surface and supporting plates, which reduces the effective axial loading force, and (2) biaxial stress state. Analytical schemes for making corrections for each of these have been presented by Balakrishnan (1999) and Boger et al. (2005), as discussed below.

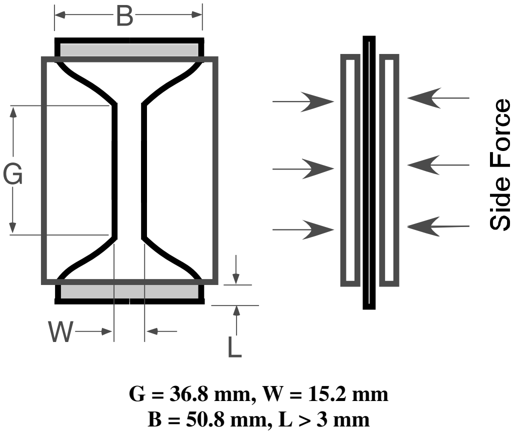

Fig. 3. Geometry of T/C test and sample dimensions (Boger et al., 2005).

Friction is minimized mechanically by sandwiching 0.35 mm Teflon® sheet between the specimen and side plates, and by applying the side force through freely turning rollers. The remaining friction force, F_f, can be estimated using a Coulomb friction law (Wagoner and Chenot, 1996):

$$F_{\mathrm{f}} = 2\mu F_{\mathrm{side}} \tag{4}$$

where F_{side} is the side supporting force and μ is the up-to-now unknown friction coefficient. The friction force must be subtracted from the measured force to obtain the effective force.

The unknown friction coefficient, μ, Eq. (4), is fit for each test utilizing side support as follows. Two identical test specimens are tested at the same rate using (a) standard tensile testing techniques (i.e. with side support), and (b) tensile testing with side support at given side loading. The side-loaded tensile curve is first corrected for biaxial tension, then is compared with the standard tensile curve. These two curves are brought into registry by adjusting μ until they coincide. This value of μ is then used to correct compression or cyclic tests of similar specimens tested at the same rate using the same side force. For the experiments presented in this paper, the friction coefficients ranged from 0.05 to 0.09. Details of the correction procedures have been presented elsewhere (Boger et al., 2005).

The correction for biaxiality is simpler and much smaller than that for friction, Fig. 4. The side force is converted to a stress using the area of the specimen in contact with the side plates, and a Von Mises yield criterion (or other choice) is used to find the equivalent tensile stress for the biaxial state. Previous work showed that the choice of yield function has a minimal effect on this correction (Boger et al., 2005).

2.4. Simple shear test

A recently devised simple shear test (Rauch and Schmitt, 1989; Rauch, 1998; Lopes et al., 2003), shown schematically in Fig. 5, provides an alternate stress state for testing that avoids the strain limitation caused by tensile necking. A set of specially designed fixtures assures that there is little axial extension of the specimen and that the clamped edges

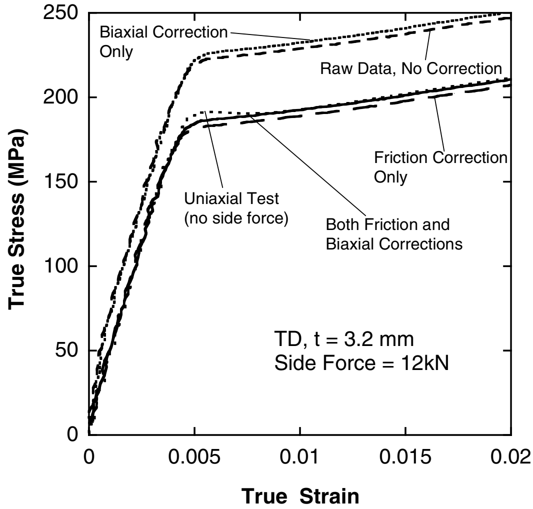

Fig. 4. Raw and corrected tensile hardening from uniaxial tensile test and test with stabilizing side plate force.

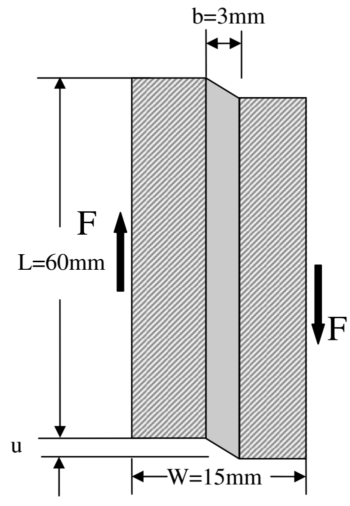

Fig. 5. Geometry and dimensions of the simple shear test.

remain parallel and at nominally fixed distance apart, thus producing simple shear. Simple shear tests were conducted at a nominal initial equivalent tensile strain rate of 2.4×10^{-3}/s at a constant crosshead speed. Strain is computed from the output of a special mechanical extensometer that records the relative axial displacement of the edges of the deformed region on the specimen. The gage length of the extensometer is 2.0 mm while the sample width is 3.0 mm between the grips, so the effect of any slipping at the grips on the measured strain is negligible. The shear stress σ_{12} and engineering (not tensor) shear strain γ_{12} are calculated as follows:

$$\sigma_{12} = \frac{F}{L \cdot t}, \quad \gamma_{12} = \frac{u}{b} \tag{5}$$

where t is the sheet thickness.

2.5. Metallography and texture measurement

Samples used for optical metallography were cut from the gauge regions where the material was deformed uniformly. Specimens were mounted and successively ground and polished, finishing with 1 μm diamond paste in ethanol. Acetic picral solution (4.2 g picric acid, 10 ml acetic acid, 70 ml ethanol and 10 ml water) was then used to etch for 5–10 s. Care was taken to etch and examine specimens immediately after polishing to avoid oxidation effects. Polishing in some cases produced surface porosity, consistent with reports in the literature (Perez-Prado and Ruano, 2002).

Crystallographic texture measurement was performed by X-ray reflection using a Scintag X1 diffractometer with Cu Kα radiation at 40 kV and 35 mA. Mid-section surfaces were used because examination showed that sheet surface textures differed from the central portion. Samples were ground to the mid-section of the sheet using standard metallography polishing procedures, finishing with 1 μm diamond paste, and then dipped into 10–20% nital (nitric acid in methanol) for 60 s to remove the mechanical damage from grinding (Agnew, 2005). Pole figures for (0002), $(10\bar{1}0)$ and $(10\bar{1}1)$ were calculated and generated using popLA software (Kallend et al., 1991).

2.6. Acoustic emission

Acoustic emission (AE) technology is a non-destructive testing method used widely in industry for detecting leakage in vessel and pipe systems. The internal structure evolution, such as crack growth, dislocation slip and twinning, can also be monitored during plastic deformation (Huang et al., 1998). In recent years, deformation of magnesium alloys has been studied using AE (Chmelik et al., 2002a,b; Bohlen et al., 2004a,b; Lamark et al., 2004). Two types of AE signal, burst AE and continuous AE, can often be distinguished in AE analysis. The start and end of a burst signal can be distinguished from background noise, in contrast to a continuous signal. A burst-type AE signal with variable (Toronchuk, 1977) amplitude is identified with twinning (Friesel and Carpenter, 1984a,b; Bohlen et al., 2002), in contrast to the continuous (Friesel and Carpenter, 1984a,b), much less intense (Skalskyi et al., 2003) AE signal corresponding to dislocation slip. The AE signal is dominated by the formation of twins (Heiple and Carpenter, 1987), i.e. the nucleation of twins rather than their growth (Toronchuk, 1977).

In situ AE measurement was performed during selected mechanical tests using a Vallen-Systeme AMSY4 AE workstation (Reed and Walter, 2003) and a Deci PICO-Z acoustic sensor with a Vallen-Systeme AEP3 preamplifier (Reed and Walter, 2003) mounted outside of the gage length of each specimen. The acoustic threshold was set immediately prior to each test at a level just above ambient noise. Other system parameters include: 40 db pre-amplifier gain, rearm time of 4 ms and duration discrimination time of 400 μs.

AE signals may be analyzed in a variety of ways. Cumulative AE count (Toronchuk, 1977), AE time count rate (Friesel and Carpenter, 1984a,b; Bohlen et al., 2002) and strain count rate were used to analyze the mechanism of the mechanical response. Cumulative

AE count is the sum of the counts of all AE events. It is associated with the extent of twin formation in the material (Bohlen et al., 2002). AE time count rate or strain count rate are the time or strain derivative of the AE cumulative count, and are similarly associated with the rate of twin nucleation.

3. Results

The deformation mechanisms of Mg have been reported as outlined in Section 1, as has the mechanical response of textured Mg sheet under either monotonic or small-strain cyclic deformation. The testing reported here seeks to clarify the evolution of hardening under large-strain non-proportional deformation paths (specifically, reverse tension/compression paths).

3.1. Monotonic tension and compression tests

Large asymmetry of yield and hardening evolution is evident in monotonic tensile and compressive tests, Fig. 6, consistent with reports in the literature (Ball and Prangnell, 1994; Nobre et al., 2002; Noster and Scholtes, 2003; Yukutake et al., 2003; Barnett et al., 2004). With the exception of the larger compressive strains attainable for the thicker material, there is little difference between the two thicknesses. While the tensile curves exhibit the standard concave-down appearance (i.e. steadily decreasing hardening rate), the compressive curves exhibit an unusual concave-up aspect. An inflection is just discernible at the limit of attainable strain for the 6.4 mm thick specimens, at approximately 0.08 strain. The various tensile yield stresses show considerable in-plane anisotropy, as shown in Table 3. An anisotropy ratio for yield stress defined by the ratio of the yield stress in the transverse direction (the largest one measured) to that in the rolling direction (the smallest one measured) is 1.17 (0.2% offset) or 1.14 (0.4% offset).

The unusual compressive behavior is related to the activation of twinning by in-plane compression (Ball and Prangnell, 1994; Nobre et al., 2002; Yukutake et al., 2003; Barnett et al., 2004), as will be shown later. The yield stress anisotropy ratio in compression is 1.06 (0.2% or 0.4% offset), considerably smaller than that for the slip-dominated deformation in tension. Comparison of Fig. 6a with b reveals only insignificant differences between the mechanical responses of the AZ31B material of various thicknesses. In the remainder of this paper, results will be shown for only one thickness unless a significant difference was noted.

Plots of width strain (measured directly) and thickness strain (determined as described in Section 2 from width and axial strains), Fig. 7a, can be used to determine the evolution of the plastic anisotropy ratio, or *r*-value, Fig. 7b. Cubic curves are fit to the data shown in Fig. 7a, as shown, and are used to determine both the cumulative *r*-value and the instantaneous one. The cumulative *r*-value (i.e. determined from total strains) is more typically reported while the instantaneous *r*-value (determined from incremental strains along the path) is of more direct interest for plasticity formulations via the normality rule. The cumulative *r*-values shown in Fig. 7b are similar to ones measured elsewhere for AZ31B (Avery et al., 1965; Agnew, 2002; Agnew and Duygulu, 2005).

Contrary to the expectation for most cubic metals, Fig. 7b shows considerable evolution of plastic anisotropy ratios (*r*-values) in tension, particularly in the TD. This

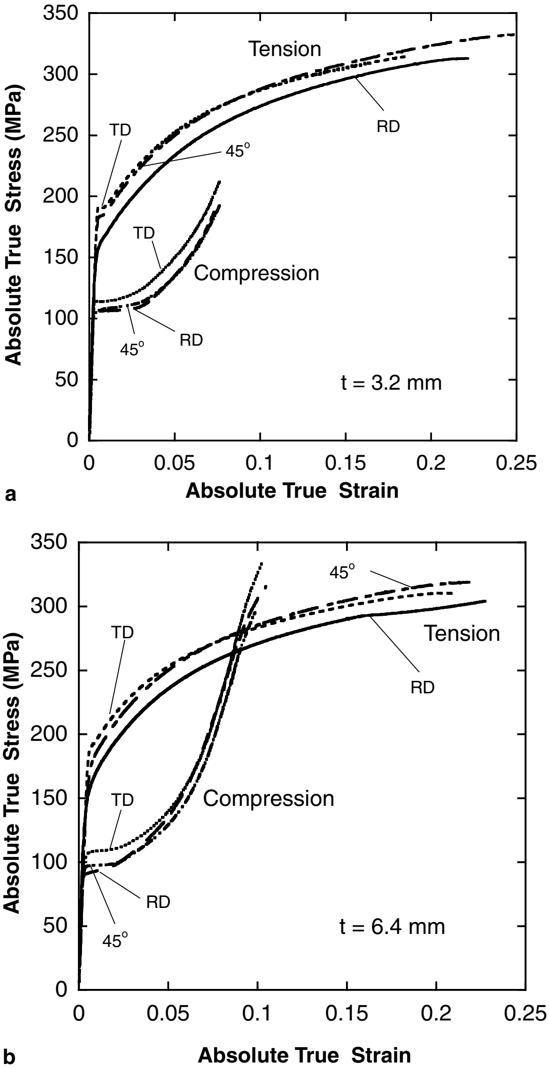

Fig. 6. Uniaxial hardening in tension and compression in three directions: (a) 3.2 mm thick material, (b) 6.4 mm thick material.

Table 3
In-plane yield and strain anisotropy of AZ31B Mg alloy

	RD	45°	TD	σ_{TD}/σ_{RD} or r_{TD}/r_{RD}
$\sigma_{yield}^{tension}$ (0.2% offset)	164 MPa	180 MPa	192 MPa	1.17
$\sigma_{yield}^{compression}$ (0.2% offset)	104 MPa	105 MPa	110 MPa	1.06
$\sigma_{yield}^{tension}$ (0.4% offset)	167 MPa	182 MPa	191 MPa	1.14
$\sigma_{yield}^{compression}$ (0.4% offset)	106 MPa	107 MPa	112 MPa	1.06
$r_{tension}^{cumulative}$ $(0 \sim 0.074)$	1.7	2.6	4.3	2.5
$r_{compression}^{cumulative}$ $(0 \sim -0.074)$	0.2	0.25	0.4	2.0

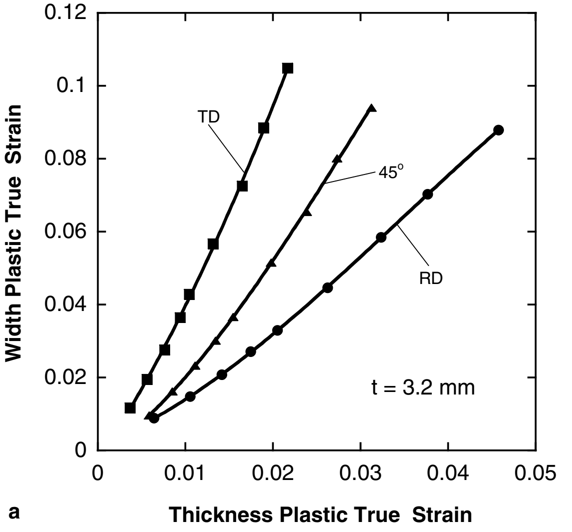

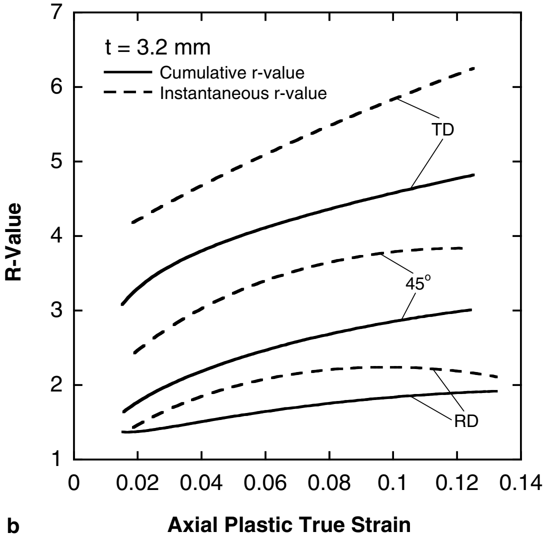

Fig. 7. Evolution of r-value with tensile strain. (a) Relationship between axial strain and width strain; (b) cumulative r-value and instantaneous r-value.

evolution has been related to a transition from basal slip to non-basal slip (Avery et al., 1965; Agnew, 2002; Agnew and Duygulu, 2005; Horton et al., 2005b). Fig. 7b and Table 3 also show considerable in-plane anisotropy of strain ratios, with anisotropy ratios of 2.5 in tension, and 2.0 in compression (over a cumulative plastic strain range of 0 to $\pm$0.074). In summary, the yield and plastic strain anisotropy are larger in tension than in compression, and anisotropy evolves remarkably rapidly compared with that of cubic metals that do not exhibit twinning.

3.2. Cyclic tension/compression tests

Large-strain compression–tension-compression (C-T-C), Fig. 8, and tension–compression-tension (T-C-T) tests, Fig. 9, were conducted for 3.2 mm thickness sheet in three directions. Figs. 6, 8 and 9 illustrate the similarity of stress evolution among the three tested directions, although there are differences in yield stress related to textural anisotropy as discussed later. Subsequent plots will focus on a single direction unless significant difference was noted.

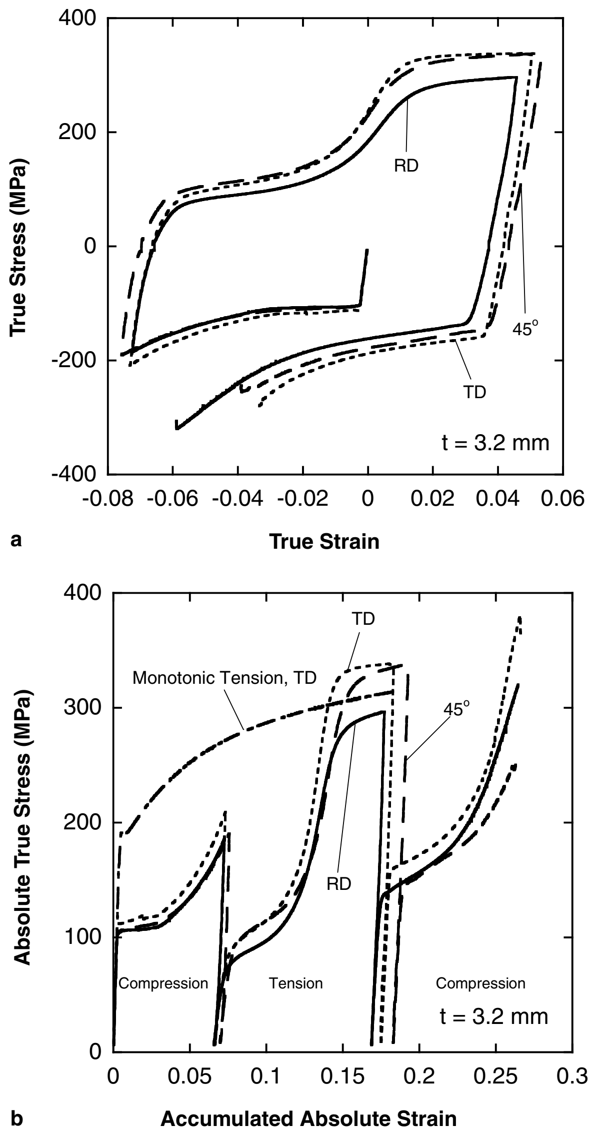

Fig. 8. Single-cycle strain hardening for C-T-C. (a) True stress vs. true strain; (b) absolute true stress vs. accumulated absolute strain.

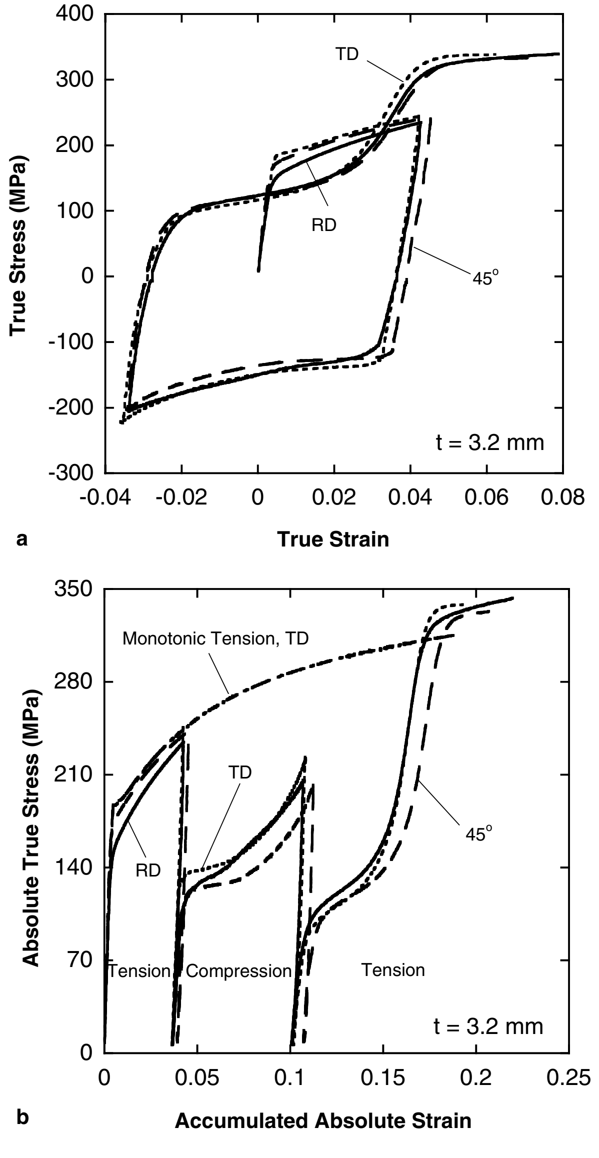

Fig. 9. Single-cycle strain hardening for T-C-T. (a) True stress vs. true strain; (b) absolute true stress vs. accumulated absolute strain.

Figs. 8b and 9b are replotted versions of Figs. 8a and 9a, useful for revealing the evolution of hardening. In these alternate plots, the absolute stress is shown, that is, compressive stresses are shown with reversed sign. Instead of standard true geometrical strain, the absolute value of each strain increment is summed to produce an accumulated absolute strain, ε_{abs}:

$$\varepsilon_{abs} = \sum_{i=1}^{n} |\varepsilon_i| \tag{6}$$

where ε_i refers to the strain accumulated in each of the n proportional-path segments of the test. Plots in the form of Figs. 8b and 9b may readily be compared to those expected for those obeying standard material models, i.e. those with isotropic hardening and symmetric yield (tension identical to compression). Under those conditions, plots such as Figs. 8b and 9b collapse to a single curve, like that shown as "monotonic tension", with elastic unloading and loading excursions whenever the stress state is reversed. The very dramatic departure of AZ31B from this "standard", or idealized, behavior is apparent.

The C-T-C tests reveal an inflected tension portion following the compressive prestrain, an effect notably absent in the monotonic tensile tests. Similarly, the T-C-T tests show no inflection upon initial tensile deformation, but the inflection appears during compression and subsequent tension. In all cases, the inflected hardening curve is accompanied by yield stresses considerably less than those for the "normal" hardening behavior. The low flow stress appearing in tension after initial compression indicates that the asymmetry between monotonic tension and compression is not related to hydrostatic pressure.

Multiple-cycle uniaxial tests were conducted using strain control for better cycle-to-cycle reproducibility. Strain ranges of 0.04 and 0.07 were set. All tests started with tension, and cycles were numbered starting from the first point of maximum compressive strain. (The initial tension and compression are labeled Cycle 0.)

Fig. 10 shows selected cycles from multiple-cycle tests. Both small and large strain amplitudes show a tendency to approach a saturated, static hysteresis loop, although in the case of large strain amplitude, fracture initiated after 10 cycles. No fracture occurs even after 20 cycles at the small strain amplitude.

The saturation behavior of the cyclic tests may be quantified by the evolution of the maximum stress ($\sigma_{\max}$, positive in tension), the minimum stress ($\sigma_{\min}$, negative in compression), and the stress amplitude ($(\sigma_{\max} - \sigma_{\min})/2$), Fig. 11. The stress amplitude for both strain ranges saturates within 3–5 cycles. For the small-strain-range test, the maximum and minimum stresses saturate in a similar period. For the large-strain-range test, the minimum stress continuously increases while the maximum stress first increases, then decreases such that the average stress decreases continuously at large strains. This behavior may be related to damage evolution which reduces the tensile strength while having less effect on the compressive strength. The fact that the large-strain amplitude specimens fracture in tension at the 10th cycle tends to agree with this interpretation.

3.3. Simple shear test

In-plane simple shear is of interest for testing of basal-textured AZ31B Mg sheet because the in-plane principal strains nominally are opposite and equal, thus producing ideally zero thickness strains. However, measurement in Mg sheet shows that small through-thickness extensile strains, 0.02, occur during the initial deformation in simple shear. Fig. 12 shows a typical result for simple shear in the RD. TD and 45° have similar flow curves as RD. Yield occurs at an equivalent tensile stress of $\bar{\sigma} = \sqrt{3}\sigma_{12} = 175$ MPa (0.2% offset). An equivalent tensile strain, $\bar{\varepsilon} = \gamma_{12}/\sqrt{3} = 0.13$, less than the tension limit, is attained before fracture. Up to a strain of approximately 0.05, strain hardening is minimal, with more rapid hardening thereafter. At a monotonic equivalent tensile strain of $\bar{\varepsilon} = 0.13$ the equivalent flow stress is 302 MPa. Upon reversal of shear, a significant Bauschinger Effect appears.

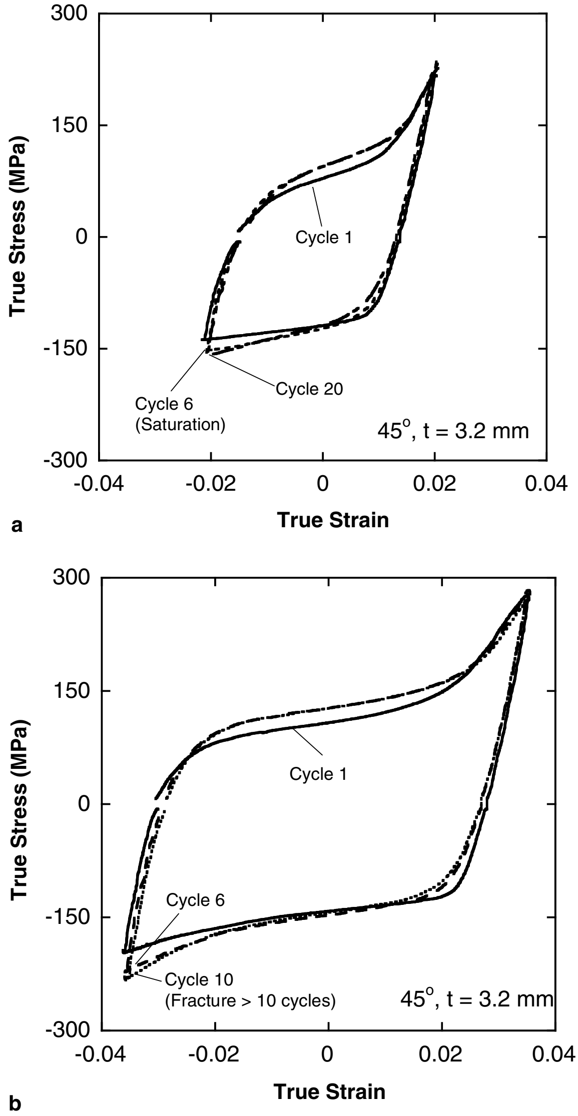

Fig. 10. Multiple cycle tests. (a) Small strain, 0.04; (b) large strain, 0.07.

3.4. Microstructure evolution

Fig. 13 summarizes the microstructure evolution for several strain states. The initial microstructure of AZ31B Mg alloy after annealing is free of twins. At a uniaxial tensile strain of 0.075, a small number of twins are arranged in needle-like narrow bands in some grains, most of the grains being twin-free. The areal fraction of twins is estimated by an average of three measurements from micrographs taken at three places on the sample by two independent researchers. Based on the multiple observations, the uncertainty of

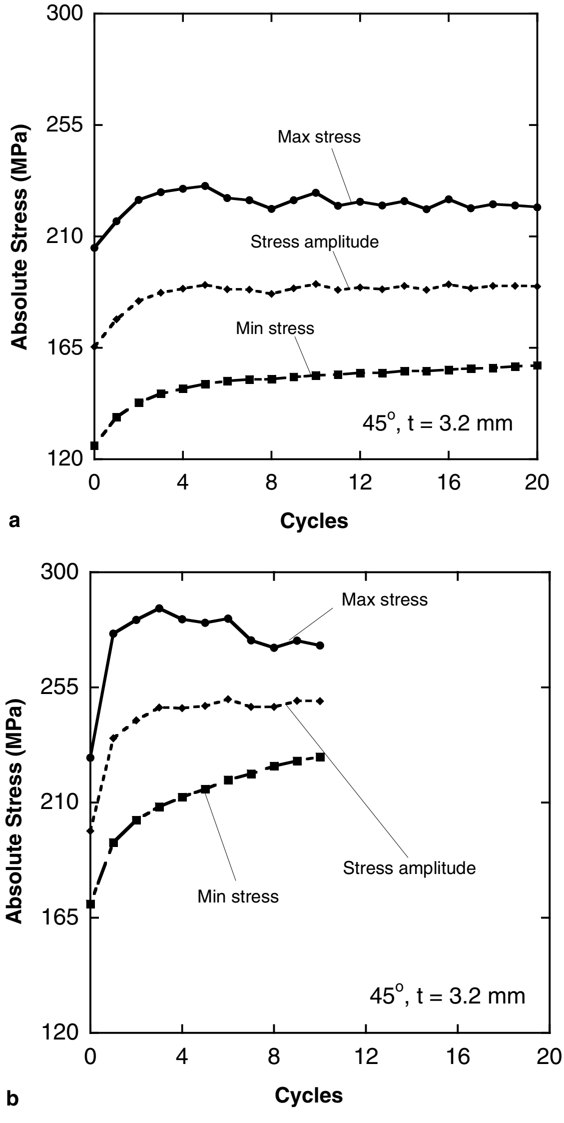

Fig. 11. Relationship between the stress and cycle number. (a) Small strain, 0.04; (b) large strain, 0.07.

the area measurement is estimated to be ±5% for larger twin fractions. The uncertainty arises when twins intersect and it becomes difficult to distinguish twinned from untwinned regions. At a tensile strain of 0.075, an areal fraction of 4% of the material is twinned, consistent with measurements reported in the literature (Koike, 2005).

When the material is loaded compressively, more twins in wider twin bands are observed. The areal twin fraction increases from 26% ($\varepsilon = -0.023$), to 58.4% ($\varepsilon = -0.046$), to 71.9% ($\varepsilon = -0.072$), similar to the reported results obtained using a neutron diffraction technique (Brown et al., 2005). This consistency suggests that the side-supporting force from the experimental fixture does not significantly suppress twinning

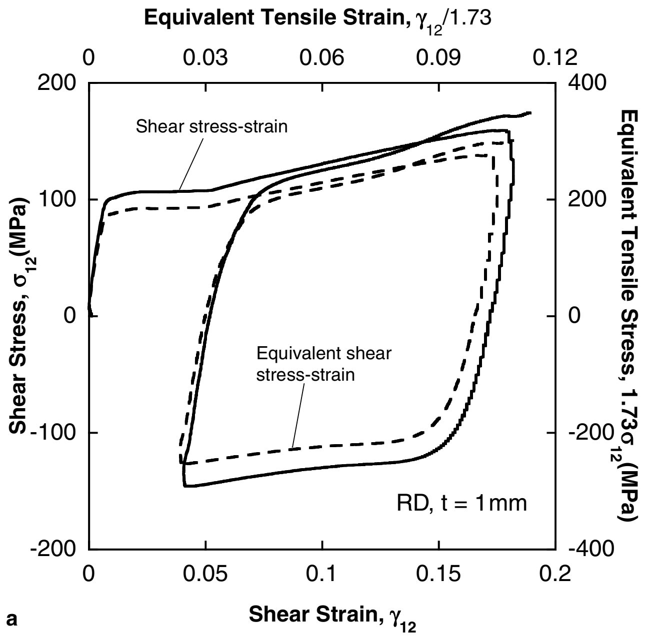

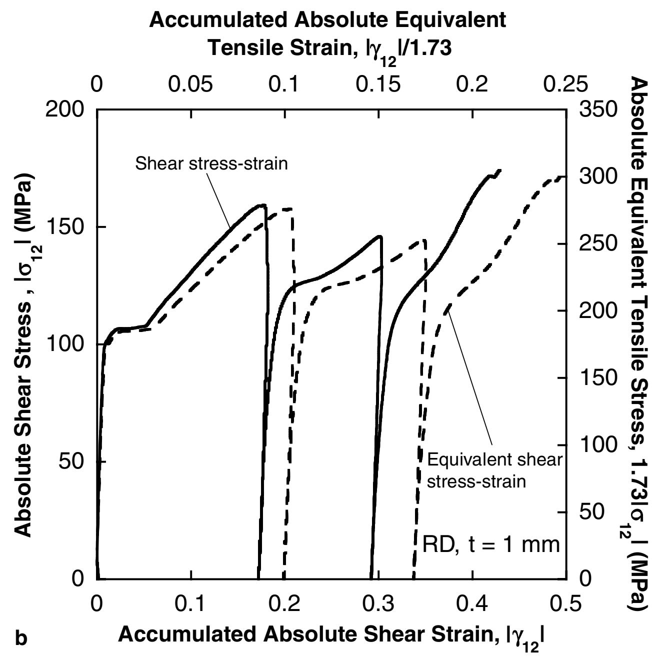

Fig. 12. Cyclic simple shear test results. (a) True stress–strain; (b) Effective stress–strain.

activity. Upon subsequent reverse tension to 0.04 strain, the wide twin bands formed during compression progressively disappear. Needle-shaped twins, similar to those observed in monotonic uniaxial tension, appear in the material. The areal fraction of twins drops

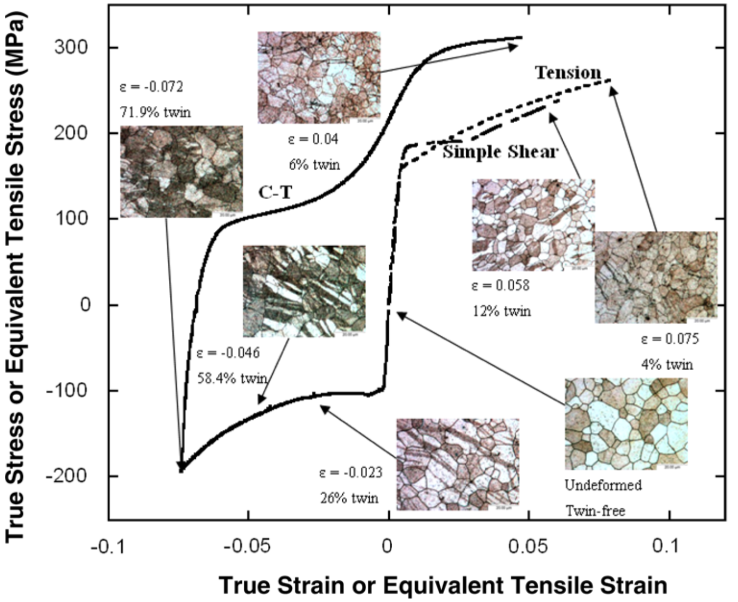

Fig. 13. Evolution of microstructure under various loading paths.

to about 6%, slightly larger than that of monotonic tension. As shown in Fig. 13, twinning also occurs in monotonic simple shear, although at a slower rate than compression. Wide-band twins, similar in morphology to the compressive twins, can be readily identified.

3.5. Texture evolution

Fig. 14 illustrates the evolution of crystallographic texture during uniaxial tension and C-T tests. The scale indicates the diffraction intensity normalized to the randomly distributed intensity, i.e. a value of 1.0 indicates the average intensity of random texture. The initial texture of the annealed magnesium AZ31B sheet alloy is shown in Fig. 14a. The (0002) basal pole figure exhibits a strong basal texture, with the majority of *c*-axes aligned in the sheet normal direction. There is some spreading of the basal pole along the rolling direction and no preferred orientation for the prismatic plane $\{10\bar{1}0\}$ or pyramidal plane $\{10\bar{1}1\}$. As shown in Fig. 14b and reported in the literature, tensile straining does not alter the basal texture significantly (Agnew and Duygulu, 2003, 2005). After in-plane compression along the rolling direction, Fig. 14c, the basal pole moves to the rolling direction (i.e. the compression axis). Fig. 14d is the texture after the subsequent reverse tension along the rolling direction; it has a strong basal texture similar to the initial, annealed material.

3.6. In situ acoustic emission

Figs. 15a and b show the cumulative acoustic emission count and time count rate during a T-C test. During the initial tension, the count rate is small, less than 10^4/s. During

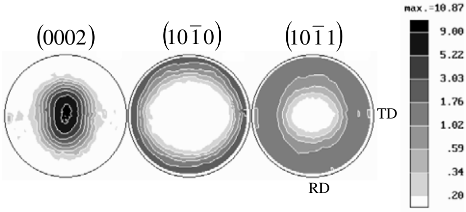

(a) Initial texture

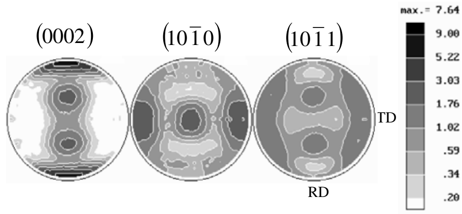

(c) Texture after compression along RD (0.07 compressive strain)

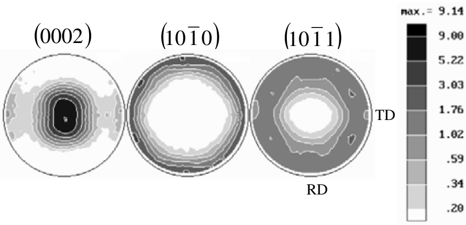

(b) Texture after tension along RD (0.1 tensile strain)

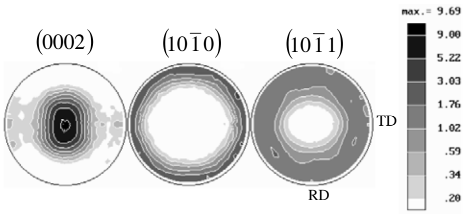

(d) Texture after reverse tension along RD (0.1 reverse tensile strain after compression)

Fig. 14. Crystallographic texture in various deformation stages. The scale at right indicates the relative diffraction intensity (1.0 = random).

subsequent compressive yield, the count rate increases dramatically, and two strain ranges with intense count rate are exhibited. The AE results are consistent with the metallographic sections, pole figures and literature. Very limited twinning takes place during in-plane tension starting from the initial texture. Upon in-plane compression, however, a rapid burst of twin creation occurs over a strain range of 0 to −0.02, followed by lower rate from −0.02 to −0.05, followed by another burst from −0.05 to −0.07 (the largest compressive strain attained in this test). It appears that there are two activation stresses for twinning in this alloy, either related to two twin mechanisms or two sets of twin orientations. Rapid strain hardening accompanies the accumulated twin production, consistent with the role of twins as slip obstacles (Yoo, 1981).

Figs. 16a and b present AE and stress–strain results for a C-T test. Similar to the foregoing T-C test, initial compression induces two bursts of high twin rate separated by a region of low twin rate. Again, the accumulated twin production is accompanied by high strain hardening. The reverse tension hardening occurs at a much lower stress than initial compression curve. This is consistent with the metallographic results showing the removal of twins throughout this region, or "untwinning" presumably without the large nucleation stress needed for twinning. However, the AE data shows only minimal activity in this region, similar to that for initial tension. Apparently the untwinning operation produces much lower acoustic signals than the twinning operation, which would be consistent with a lower activation stress.

A few T–C–T and C–T–C tests were preformed as acoustic emission was recorded. The final compressive leg of the C–T–C tests show acoustic emission count rates that fall between those for initial twinning (initial compression) and for slip (initial tension) or untwinning (tension after compression), Fig. 17. The final compression leg initially shows

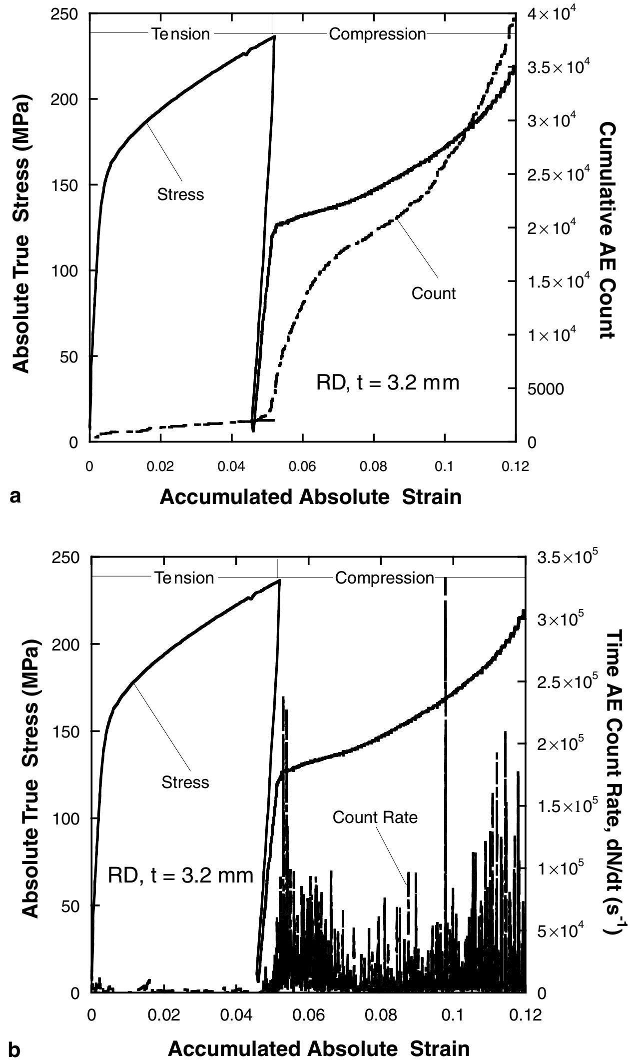

Fig. 15. Acoustic emission during T-C test. (a) Cumulative AE count; (b) time AE count rate.

count rates two or three times the minimal ones for untwinning or slip, but these rise toward the end of the leg to become one-third to one-half those for initial twinning.

4. Discussion

The foregoing experiments show that significant asymmetric yield and hardening behavior is exhibited in magnesium AZ31B sheet alloy at room temperature. An inflected and concave strain hardening flow curve was observed in both compression and reverse tension. A large Bauschinger Effect occurs during cyclic testing or simple shear testing. As has been widely reported in the literature, the origin of these effects lies in the activation of twinning under certain loading conditions.

a
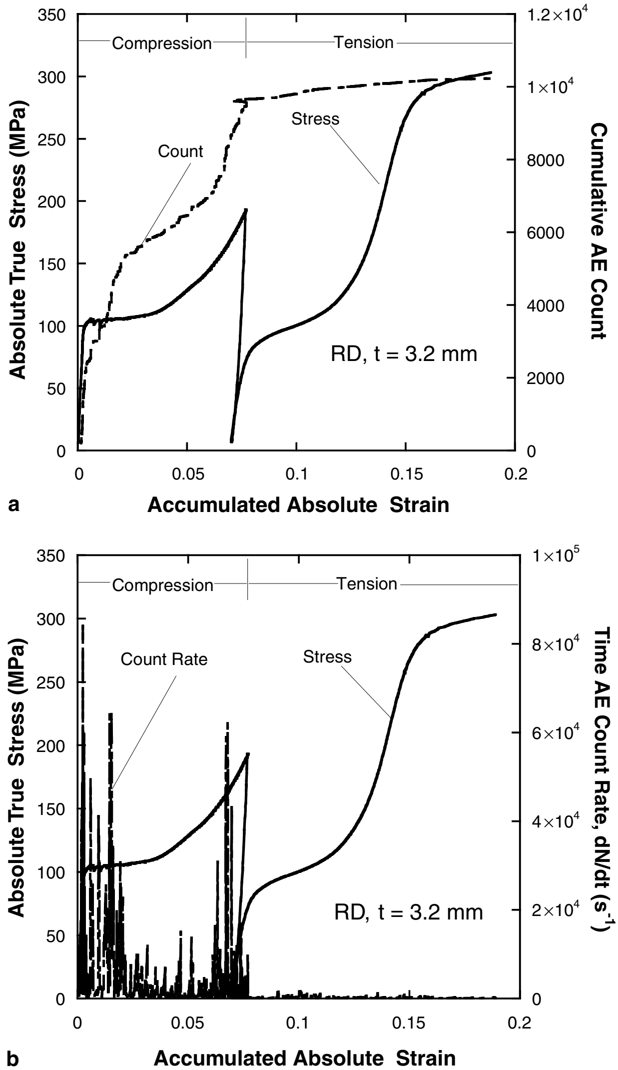

Fig. 16. Acoustic emission during C-T test. (a) Cumulative AE count; (b) time AE count rate.

4.1. Mechanisms of deformation and consequences

As discussed in Section 1, the easily activated $\{10\bar{1}2\}$ twin found in Mg alloys is a 'tension' twin, i.e. one which can be activated by extension parallel to the c-axis in a HCP crystal structure (Roberts, 1960; Partridge, 1967; Kelly and Hosford, 1968; Yoo, 1981), or equivalently, by in-plane compression (Reed-Hill and Abbaschian, 1994). The initial crystallographic texture of AZ31B magnesium sheet alloy exhibits a strong basal texture, where the majority of c-axes are aligned in the sheet normal direction with some spreading in the rolling direction, the prismatic planes $\{10\bar{1}0\}$ and pyramidal planes $\{10\bar{1}1\}$ are randomly distributed in the sheet plane initially.

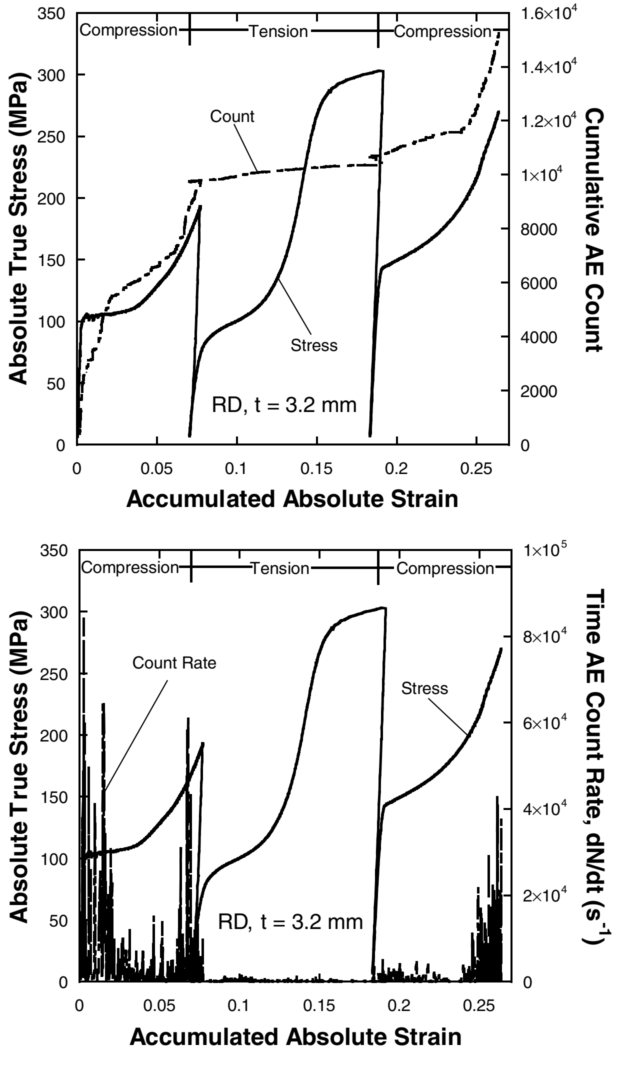

Fig. 17. Acoustic emission during C–T–C test. (a) Cumulative AE count; (b) time AE count rate.

An in-plane compressive stress results in twinning, while in-plane tension with a contraction along *c*-axes does not. Therefore, optical microscopy shows only a small number of local, narrow band twins after in-plane uniaxial tension. These twins are produced under tension stress state because even in the highly textured sheet the *c*-axis orientation of some grains may be aligned with the loading direction, or because of stress state inhomogeneities introduced by inter-grain interactions (Koike, 2005). It should be noted that a spreading of basal pole along the rolling direction allows easier activation of basal slip by RD tension. The strong basal texture in TD requires activation of non-basal slip, which increases the yield stress. The higher incidence of non-basal $\langle a \rangle$ slip relative to basal $\langle a \rangle$ slip during TD tension is responsible for the higher *r*-value of TD than that of RD and 45° (Agnew and Duygulu, 2003). Under tension, there is little thickness strain, but the activity of non-basal $\langle a \rangle$ slip produces large width strain, thus a large r-value (Koike, 2005). During tension, non-basal slip is progressively activated as the stress increases, thus the r-value increases with tensile strain.

After in-plane compression along RD, significant wide-band twins appear and the basal pole of the texture shifts rapidly to the rolling direction. This is characteristic of $\{10\bar{1}2\}$ twinning, which rotates the c-axes toward the compressive loading direction. An areal fraction of 71.9% twinned area is observed at a compressive strain of 0.072. Twinning produces significant thickness strain in compression, thus, the compressive r-values in all three directions are smaller than 1. For pure twinning deformation under in-plane compression of a perfectly c-texture sheet with random axis orientations in the plane, an r-value of -0.09 is expected, as demonstrated in Appendix. An overall small, positive r-value for compression reflects the contribution of slip to the total deformation. Because of the exhaustion of twinning and dominance of slip at large compressive strain, compressive r-values increase with compressive strain.

Subsequent in-plane tension produces an extension along the c-axes of these newly aligned crystals, activating an untwinning process. Untwinning rotates the c-axes of untwinned regions back to the sheet normal direction, thus the strong basal texture again appears in the texture. The microstructure shows that the originally formed wide-band twins disappear, instead, only a few narrow-band twins remain, similar to the uniaxial tensile condition. Untwinning removes the original twins and produces the reverse of the previous strain caused by twinning. From the metallographic and texture evidence, it is clear that, untwinning is the critical mechanism during subsequent tensile deformation (i.e. following compression) as opposed to nucleation and growth of new twins in alternate orientations. The untwinning flow curve is very similar in appearance to the original compression curve, i.e. with a sigmoidal aspect having an inflection.

4.2. *Working model of deformation mechanisms*

A working model of the deformation mechanisms under reverse loading may be constructed consistent with the experimental results presented here and with those appearing in the literature (Staroselsky and Anand, 2003; Yukutake et al., 2003). (A "working model," as used here, is a conceptual framework of which some aspects are subject to experimental verification.) The conceptual result is shown schematically in Fig. 18 for three strain paths: monotonic tension, monotonic compression, and reverse tension following compression. The first and last of these are experimental ones, with the monotonic compression curve being a composite curve, derived as outlined below.

As shown in Fig. 18, the initial plastic modulus at yield in tension (after a brief yield point phenomenon presumably related to twinning) is approximately 2000 MPa. This slope may be conveniently used to identify two other characteristic points on the stress–strain curves. When associated with concave-up curvature, it represents a mid-point between twin-dominated and slip-dominated flows. When associated with concave-down curvature, it signals the end of the twin-facilitated flow and may be used to characterize slip resistance, or "slip-dominated flow stress".

The composite monotonic compression curve consists of a first experimental portion and second portion translated from an experimental reverse tension curve (which extends the attainable strain range). The second curve is translated in stress and strain until the points on the two curves having 2000 MPa slopes (and concave-up curvature) coincide.

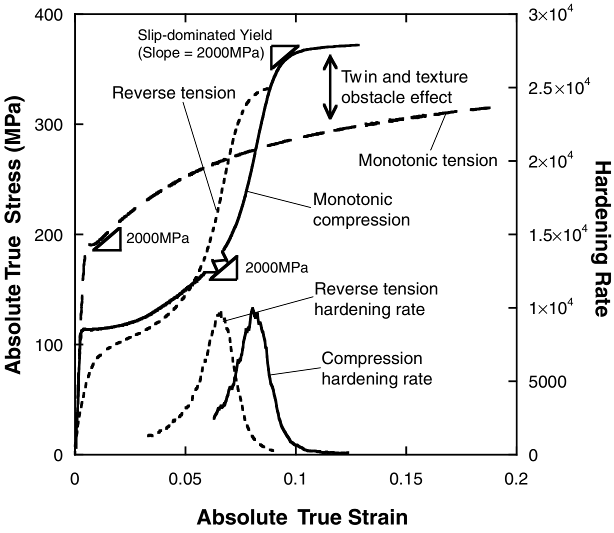

Fig. 18. Schematic of strain hardening. Note that the monotonic compression curve is a composite one, constructed as described in the text.

The working model may be described as follows. Monotonic tension exhibits the normal strain-hardening aspect encountered in non-twinning materials, although some small amount of twinning is present, as shown by metallography and AE, presumably as required for arbitrary deformation with activation of only four independent slip systems. Because twinning is difficult during in-plane tension, the constraints of the limited number of independent slip systems cause a high yield and flow stress, with hardening consistent with a predominant slip deformation.

Monotonic compression exhibits a lower yield stress and initial hardening rate than tension because twinning is facilitated. However, after a strain of approximately 0.05, the hardening rate increases rapidly as the capacity for twinning is exhausted locally within the polycrystal. The reverse tension flow curve exhibits lower yield stress than monotonic compression, consistent with reported low twin propagation stresses relative to twin nucleation stresses (Partridge, 1965; Reed-Hill and Abbaschian, 1994). Untwinning does not involve nucleation of twins, thus, the stress of untwinning is less than that of twinning (Partridge, 1965).

The simple shear test exhibits a similar, but less dramatic, flow curve. Initial yield is followed by a low hardening rate up to a strain of 0.05, at which time the hardening rate increases, giving a concave-up aspect. This appearance is consistent with twinning and concurrent slip. However, twinning cannot occur without an accompanying through-thickness extensile strain in the initially basal-texture sheet. After a simple shear strain of 0.1, the thickness strain was carefully measured and found to be 0.02 with a measurement uncertainty of ±0.007, consistent with the presence of twinning. The sheet area of the shear specimen is not constant during the deformation, as would be expected for an isotropic material or for a rigorously controlled shear test. It appears that the compliance of the fixture, or laterally slipping in the grips, allows some material contraction normal to the applied displacement. The in-plane compression resistance under a principal compressive stress is less than that of the more difficult in-plane extension under the principal tensile stress, thus favoring a net contraction in the plane and net extension through the thickness.

As discussed in the Sections 1 and 2, burst-type AE counts are associated closely with twinning events. Fig. 19 shows the experimentally measured AE cumulative counts and strain count rate from a compression test and the corresponding area twinning fraction obtained by metallographical examination. After a compressive strain of 0.05, a second stage of high count rate occurs. However, as shown in Fig. 19b, the areal fraction of twin-

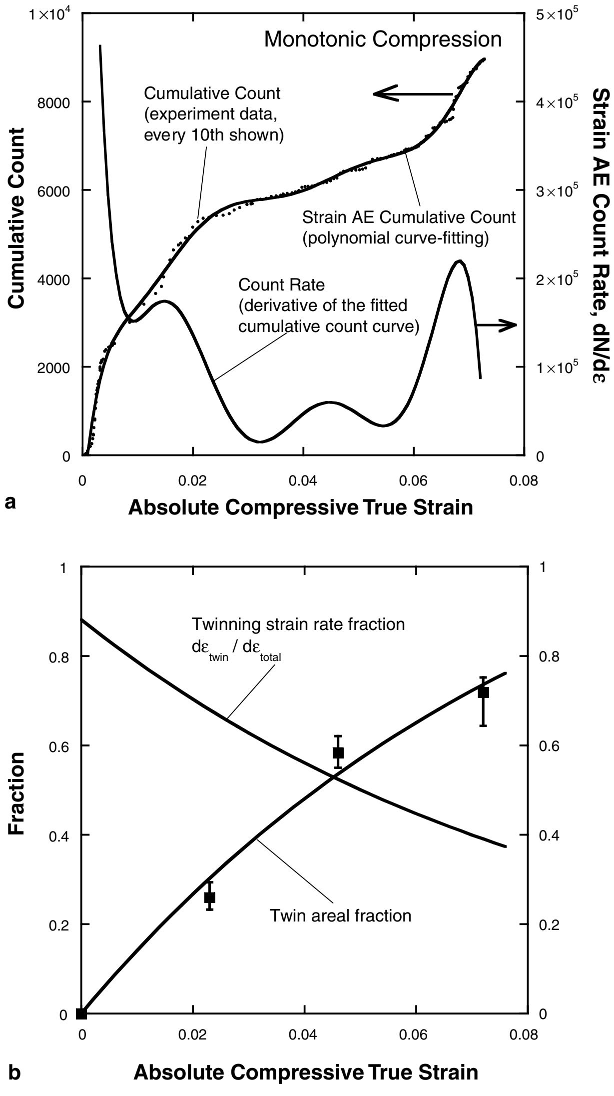

Fig. 19. Evolution of AE count and areal twin fraction with compressive strain. (a) Cumulative count and strain count rate; (b) fraction of strain rate attributed by twinning (points represent the experimental results, curves are fit as described in text).

ning increases at a steadily decreasing rate, seemingly in disagreement with the AE data. In fact, this discrepancy confirms reports in the literature (Toronchuk, 1977; Friesel and Carpenter, 1984a; Friesel and Carpenter, 1984b; Heiple and Carpenter, 1987; Bohlen et al., 2002) that the AE counts are related to twin nucleation and initiation, rather than to growth and thickening. The growth of twins has been reported to contribute to AE signals one-to-two orders of magnitude less than nucleation (Toronchuk, 1977). It is also for this reason that the AE signal for untwinning, which does not require nucleation, is quite small, Fig. 16.

With this interpretation of AE signals in mind, the strain-count-rate plot of Fig. 19a can be understood. The first peak is associated with nucleation of twins of the principal type in Mg, $\{10\bar{1}2\}$ twin. As straining proceeds, fewer new twins are nucleated because of unfavorable grain orientations and the already activated ones continue to grow without an accompanying large AE signal. As these favorable twins become exhausted, the stress rises and either a new type of twin begins to be nucleated (for example, $\{10\bar{1}1\}$ and $\{30\bar{3}2\}$ twins have been observed in large tensile strains in Mg (Koike, 2005)), or possibly unfavorably oriented grains can accommodate twinning at the high stress.

The strain rate fraction attributable to twinning plotted in Fig. 19b is computed from a curve fit to the measured cumulative twin fraction, that is, $F_{\text{twin}} = 1.3224 \cdot (1 - e^{-11.301\varepsilon})$ in Fig. 19b. A fully twinned Mg single crystal produces an compressive strain of 6.4% (Kocks and Westlake, 1967). However, for a basal textured sheet with random in-plane orientation of the $\langle a \rangle$ axes, the equivalent compressive strain is 5.9% (see Appendix A). Assuming that the areal twin fraction is proportional to the strain from twinning, the twinning strain can be computed:

$$\varepsilon_{\text{twin}} = F_{\text{twin}} \cdot 0.059 \tag{7}$$

Similarly, the slope of the twin fraction curve gives the twin fraction rate, i.e. the increase of twin fraction per unit strain, $\dot{F}_{\text{twin}}$:

$$\dot{F}_{\text{twin}} = \frac{dF_{\text{twin}}}{d\varepsilon_{\text{total}}} \tag{8}$$

and the fraction strain rate attributable to twinning is:

$$\dot{\varepsilon}_{\text{twin}} = \frac{d\varepsilon_{\text{twin}}}{d\varepsilon_{\text{total}}} = \dot{F}_{\text{twin}} \cdot 0.059 \tag{9}$$

Since the total strain rate is contributed by slip strain rate and twinning strain rate, thus

$$\dot{\varepsilon}_{\text{total}} = \dot{\varepsilon}_{\text{twin}} + \dot{\varepsilon}_{\text{slip}} \tag{10}$$

Calculations such as these, which are clearly approximate, complete the basic working model. The strain mechanisms are dominated by twinning activity in initial compression, but by slip as twinning becomes more difficult as it approaches exhaustion. A transition point between twinning and slip dominated deformation may be defined by equal slip and twinning strain rates. This occurs at a compressive strain of 0.05 in AZ31B as tested here. The flow stress is determined by the stress needed to activate all of the required mechanisms in order to maintain compatibility by providing the Von Mises-required five independent deformation mechanisms. The initial twinning activation stress is high, with twinning growth occurring more readily (and with little AE signal). However, twinning is both polar and of limited extent. In addition, twins function as obstacles to dislocation motion and twinning causes rapid textural changes that in the case of Mg cause textural softening initially. For all of these reasons, the flow stress inevitably increases as twinning proceeds, at first slowly during the growth stage. As exhaustion is approached, as a dense set of twin obstacles is established, the stress increases rapidly. Eventually, the flow stress becomes so high that local cracks are created and propagated by incompatibility caused by removing twinning from the mix of independent deformation mechanisms.

A working model has been established which accounts for the principal characteristics of monotonic and reverse deformation paths in terms of slip, twinning and untwinning. Continuous reverse tests can also reveal secondary characteristics of interest for formulating an accurate constitutive model.

4.3. Quantitative analysis of hardening mechanisms

The flow stress of a polycrystal is determined by the critical resolved shear stress of the deformation mechanisms, their orientation to the applied stress, and the role of various obstacles to the operation of such mechanisms: dislocations, solutes, precipitates, and grain/twin boundaries. Determination of the relative magnitude of these effects is not straightforward, but quantitative estimates can be made.

For the Mg AZ31B alloy tested here, the analysis is simplified because there are no precipitates, the solute content is constant, and the grain size is constant. Furthermore, by limiting the analysis to a saturated tension-compression loop (say, the 10th cycle shown in Fig. 10b, which is nearly identical to the 6th-through-9th cycles), isotropic hardening from dislocation accumulation can be avoided and thus ignored in subsequent analysis (Ohno, 1982; Kang et al., 2003). Fig. 20a shows the same data as Fig. 10b, but in terms of more convenient variables for comparison: absolute stress and absolute true strain following the stress reversal. Such a plot emphasizes the flow differences between tension and compression, and the similarity of hardening for the first strain range after the stress reversal.

To begin to separate the other effects on hardening, the stresses near the start of plastic flow in the tension and compression segments of the saturated testing cycle, σ_0^{T} and σ_0^{C}, respectively, are compared. The difference arises from various roles of twinning: (1) CRSS for twinning vs. untwinning, $\sigma_{\text{twinning}} - \sigma_{\text{untwinning}}$; (2) the obstacle effect of twins on slip, $\Delta\sigma_{\text{obstacle}}$, (3) texture hardening caused by evolution of texture, $\Delta\sigma_{\text{texture}} = \sigma_{\text{w/twins}} - \sigma_{\text{w/o twins}}$ (i.e. the difference in flow stress attributable to the difference in the twinned texture and the annealed, untwinned texture):

$$\sigma_0^{\mathrm{T}} - \sigma_0^{\mathrm{C}} = -(\sigma_{\text{twinning}} - \sigma_{\text{untwinning}}) + \Delta\sigma_{\text{texture}} + \Delta\sigma_{\text{obstacle}} \tag{11}$$

As noted above, dislocation multiplication is ignored in Eq. (11) because a) very little such multiplication is expected in saturated cycles; b) even if such multiplication did occur as straining proceeded, the symmetry of the slip situation for the two legs would produce no change in the difference $(\sigma_0^{\mathrm{T}} - \sigma_0^{\mathrm{C}})$, Eq. (11); and c) recent work has shown that dislocation multiplication does not affect the CRSS for twinning (Jain and Agnew 2006). Therefore, $(\sigma_{\text{twinning}} - \sigma_{\text{untwinning}})$ is expected to be approximately independent of strain.

The texture hardening component of Eq. (11) is related primarily to texture changes caused by twinning since texture hardening from slip evolves much more slowly and can be ignored over the small strain range considered here. (Note that $\Delta\sigma_{\text{texture}}$ is negative, Appendix B. This means that the twinned texture for which σ_0^{T} is measured is oriented

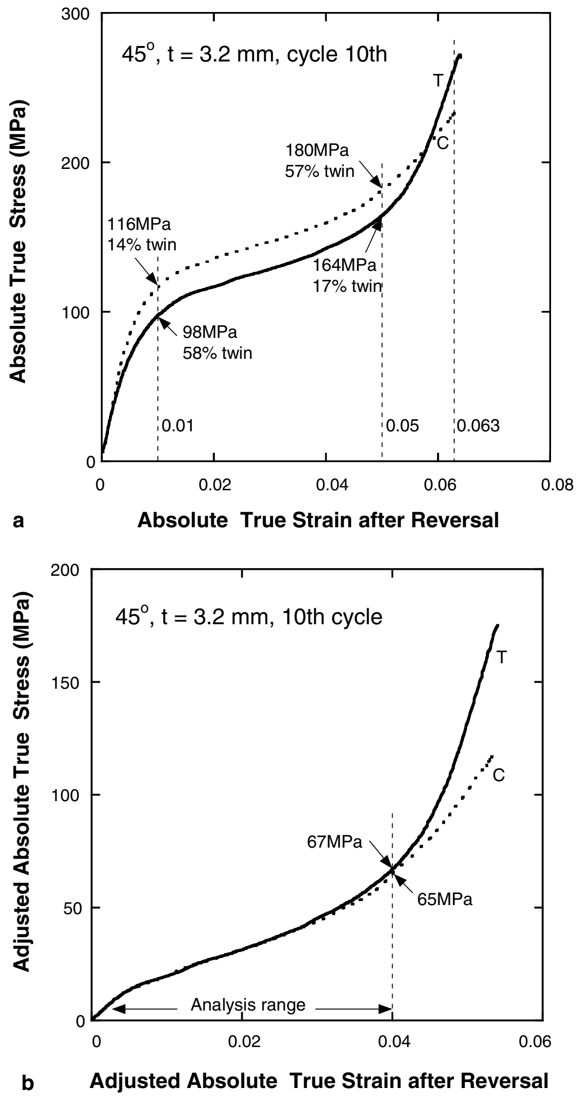

Fig. 20. Comparison of strain hardening in the 10th cycle for large strain cyclic tension and compression tests. (a) Comparison of absolute stress strain curve in cyclic tension and compression stages; (b) adjusted stress and strain for region with the same hardening rate in cyclic tension and compression stages.

more favorably for slip than is the untwinned texture for which σ_0^C is measured. Thus, twinning introduces textural softening, but may also introduce hardening by changing deformation mechanisms or by providing obstacles to dislocation motion.)

While the traditional method used to define yield is the stress at a 0.2% offset, behavior at this strain includes confounding transient effects from the stress reversal, as shown earlier. Four alternative methods were employed to identify "yield:" (1) stress at 0.004 strain offset, (2) stress at a strain of 0.01 after reversal, (3) stress at a fixed slope intermediate to elastic and plastic slopes, 2000 MPa, and (4) a back-extrapolation stress using the intersection of the extended linear region of the hardening curve with the extended initial linear elastic region. The last method is particularly convenient for this twinning material because the hardening curves for both tension and compression show a very nearly linear region with common slope of 1200 MPa over a significant strain range, Fig. 20a. As shown in Table 4, the individual yield stresses obtained by these methods differ by up to 12 MPa, but the difference between the tensile and compressive yield stresses, σ_0^T and σ_0^C, is nearly independent of method: 18–19 MPa.

The difference in strains where the yield points occur in tension and compression for each of the three methods, ε_0^T and ε_0^C, differ only slightly, from −0.0002 to 0.0002 strain, Table 4. This consistency emphasizes the role of transient yield just following stress reversal. (*Note*. The yield strains corresponding to the yield stresses obtained by the back-extrapolation method are defined by the strain at which the measured flow curves attain the yield stress.)

Adopting the predominant value of $\Delta\sigma_{\text{texture}}$ for all subsequent analysis, Eq. (11) can thus be made explicit, as follows:

$$\sigma_0^T - \sigma_0^C = -(\sigma_{\text{twinning}} - \sigma_{\text{untwinning}}) + \Delta\sigma_{\text{texture}} + \Delta\sigma_{\text{obstacle}} = -18\ \text{MPa} \tag{12}$$

Fig. 20a shows the yield stresses and strains determined by a strain of 0.01 after reversal, one of the choices compared in Table 4. Also shown on Fig. 20a are the estimated twin fractions at strains after reversal of 0.01 and 0.05 for tension and compression stages. These fractions are estimated from Fig. 19b as follows: For the compressive stage of cyclic deformation, Fig. 19b is used directly. That is, at strains of 0.01 and 0.05, the corresponding twin fractions may be obtained from the corresponding twin areal fractions shown. This assumes that the twin fraction at the start of the cycle is nearly zero, consistent with the metallographic measurement following a large tensile cycle. For the tensile stage of cyclic deformation, Fig. 19b is used starting from a strain of 0.063 and reading backwards to account for untwinning. That is, at the start of the tension stage, a twin fraction of 58% is expected based on Fig. 19b at 0.053 (=0.063 − 0.01). At a tensile strain of 0.05, a twin fraction of 17% is obtained at a strain of 0.013 (=0.063 − 0.05).

For the remaining analysis, the strain hardening over a common part of the strain range from tension and compression legs of the saturated cycle will be analyzed. Fig. 20b is a replot of Fig. 20a in terms of $(\sigma^T - \sigma_0^T)$ or $(\sigma^C - \sigma_0^C)$, and $(\varepsilon^T - \varepsilon_0^T)$. That is, Fig. 20b represents the strain hardening following the initial, transient region following the reversal, which is identical within experimental error up to a subsequent strain of 0.04. After that, the differences are presumably related to the earlier exhaustion of untwinning for the tensile curve, and consequent activation of deformation mechanisms with higher CRSS. The earlier exhaustion is expected in tension because only 70% of the available regions are indeed twinned at a compressive strain of −0.07.

Table 4
Stress and strain and their difference at starting point of parallel region in the 10th cycle of cyclic deformation

Criterion	σ_0^T (MPa)	σ_0^C (MPa)	$\sigma_0^T - \sigma_0^C$ (MPa)	ε_0^T	ε_0^C	$\varepsilon_0^T - \varepsilon_0^C$
Strain offset of 0.004	98	117	−19	0.0100	0.0102	−0.0002
Strain after reversal of 0.01	98	116	−18	0.01	0.01	0.00
Slope of 2000 MPa	110	128	−18	0.0144	0.0142	0.0002
Back-extrapolation	100	118	−18	0.0108	0.0106	0.0002

The remaining analysis compares strain hardening during tensile and compressive segments of the saturated cycle over the common strain range following reversal: 0.01–0.05 (or 0.0–0.04 range after "yield" as defined above). In terms of the definitions adopted above, the stress difference at the end of each segment may be expressed as follows:

$$(\sigma_f^T - \sigma_f^C) = (\sigma_{twinning} - \sigma_{untwinning}) - \Delta\sigma_{texture} - \Delta\sigma_{obstacle} \tag{13}$$

which may be combined with Eq. (12) and expressed explicitly using the differences shown in Fig. 20b:

$$(\sigma_f^T - \sigma_f^C) - (\sigma_0^T - \sigma_0^C) = 2\ \text{MPa} = -2\Delta\sigma_{texture} - 2\Delta\sigma_{obstacle} \tag{14}$$

Eqs. (12) and (14) have three unknowns and thus cannot be solved for the desired variables. Fortunately, $\Delta\sigma_{texture}$ can be assessed independently, Appendix B, from the textures shown in Fig. 14: $\Delta\sigma_{texture} = -10$ MPa. With this additional information, the various contributions of twinning to hardening can be deconvoluted by solving equations: $\Delta\sigma_{texture} = -10$ MPa, $\Delta\sigma_{obstacle} = 9$ MPa, and $\sigma_{twinning} - \sigma_{untwinning} = 17$ MPa. Thus, the roles of twins on texture hardening and as obstacles are of the same magnitude, while the difference between activation of twinning vs. untwinning is twice as large.

4.4. Complex reverse paths

T-C-T tests were carried out with initial tensile prestrains of various values, followed by fixed compressive and tensile strain ranges of ~0.07, Fig. 21. Raw plots like Fig. 21a are difficult to interpret directly, but may be summarized in terms of yield stresses following the transitions, Fig. 20b and c. While it is traditional to use a yield stress defined by a 0.2% offset, this value is insufficient to capture the essence of reverse yielding. Presumably because of large micro-plastic backflow of dislocations piled up at twin obstacles (Yoo, 1981; Karaman et al., 2001), low effective unloading moduli and gradually curved elastic–plastic transitions are observed upon the stress transitions. As shown in Fig. 21b, the choice among slightly larger offset yield stresses, 0.4–1.0% makes little difference, but the 0.2% offset yield stress still lies in the rapidly changing portion of the stress–strain curve.

The behavior illustrated in Fig. 20a and b is typical of all of the transitions observed. Therefore, 0.4% offset yield stresses are used for comparison hereafter. In particular, Fig. 21 shows that tensile prestrain more than 0.03 increases the subsequent compressive yield stress. The tentative conclusion is that the multiplication of dislocations in tension (and creation of a small number of local twins) creates obstacles that remain effective upon compressive loading. This presumably occurs by increasing the activation stress for twinning which, according the working model, determines the flow stress.

Fig. 21c shows the subsequent compressive yield stress and the 2nd tensile yield stress (i.e. after variable tensile prestrain, the −0.07 compressive strain) as a function of the flow stress at the end of the first tension path. While the compressive yield stress (dominated by twinning) increases markedly (50 MPa) corresponding to the pre-stress increase of 80 MPa, the second reverse tension stress (dominated by untwinning) occurs at less than half the compression value, and does not increase with pre-stress. These results indicate that dislocation multiplication affects the twin nucleation stress, but has little or no effect on the untwinning stress, which does not require nucleation. The untwinning stress is approximately half of the twinning stress.

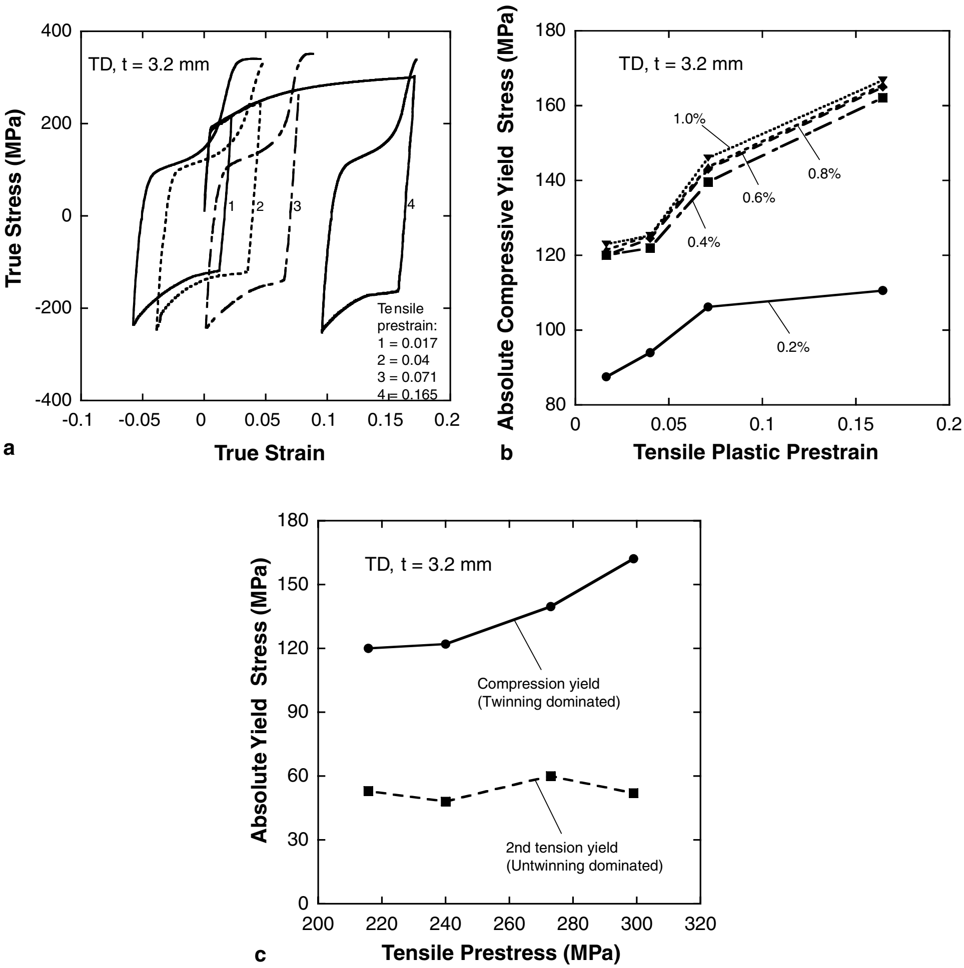

Fig. 21. Tension–compression-tension (T-C-T) results for various initial tensile prestrain. (a) Raw stress–strain data; (b) variation of reverse compressive yield stress based on several offset yield criteria; (c) variation of reverse compressive yield stress (0.4% offset) and second tensile yield stress (0.4% offset) with the final flow stress at the end of the tensile prestrain.

Fig. 22 analyzes C-T-C tests with various levels of initial compressive strain followed by fixed tensile strain and final compressive strain. Fig. 22a is the raw data and Fig. 22b relates reverse hardening parameters to initial compressive prestress (similar to Fig. 21c for T-C-T tests). Consistent with the previous T-C-T results, the tension yield (untwinning controlled after the initial compression-produced twins) is unaffected by prestrain greater than 0.03 and occurs at a value of approximately 30–50 MPa. The slip-dominated flow point (where $E_{plastic} = 2000$ MPa) in tension increases dramatically (120 MPa) with increasing compressive prestress (100 MPa), thus implying that even twinning followed by untwinning (and of course the even? large accumulated slip) leaves behind a high density accumulated slip obstacle. The final compressive yield, in spite of the wide variation of flow stress immediately prior to the reversal, is almost unaffected by the preceding cycle

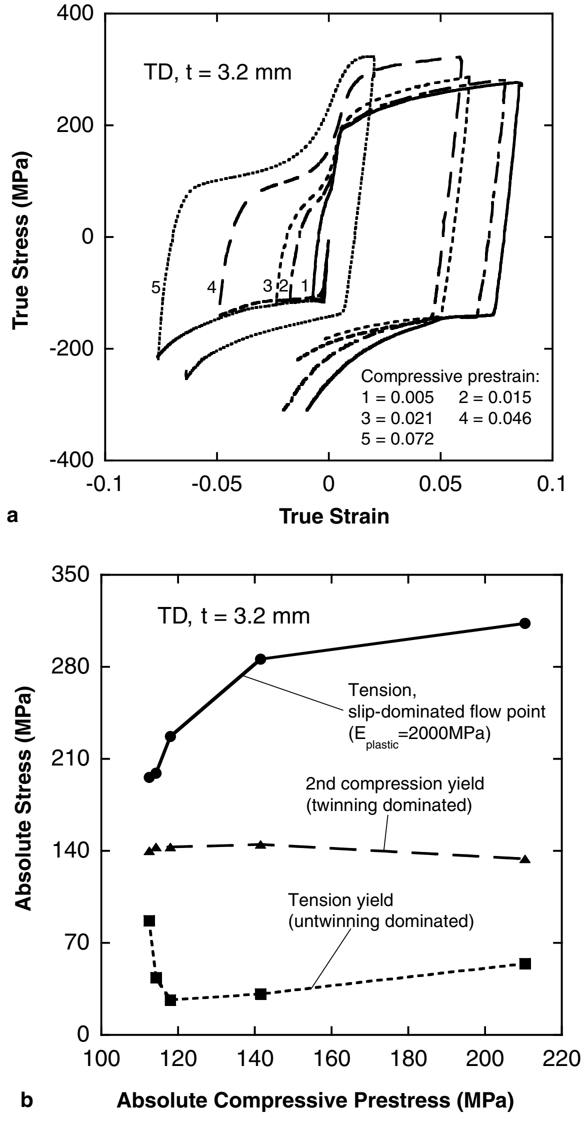

Fig. 22. Compression–tension-compression (C-T-C) results for various initial compressive prestrains. (a) raw stress–strain data; (b) variation of characteristic yield stresses (0.4% offset) and slip dominated flow points (Eplastic = 2000 MPa) with the final flow stress at the end of the compressive prestrain.

parameters, as is the subsequent hardening. It should be noted that the estimated slip activity preceding the final compression is nearly the same in all cases, consistent with the constant final compression yield stress observed.

In order to isolate the effect of untwinning better, C-T-C tests were conducted with similar compressive prestrains of 0.07, followed by tension to various strains, and then final compressive loading, Fig. 23a. The tensile part of the cycle subjects the material to more untwinning and slip. As shown in Fig. 23b, the second compressive yield stress increases (90 MPa) with increasing tensile flow stress just prior to the reversal (180 MPa). But

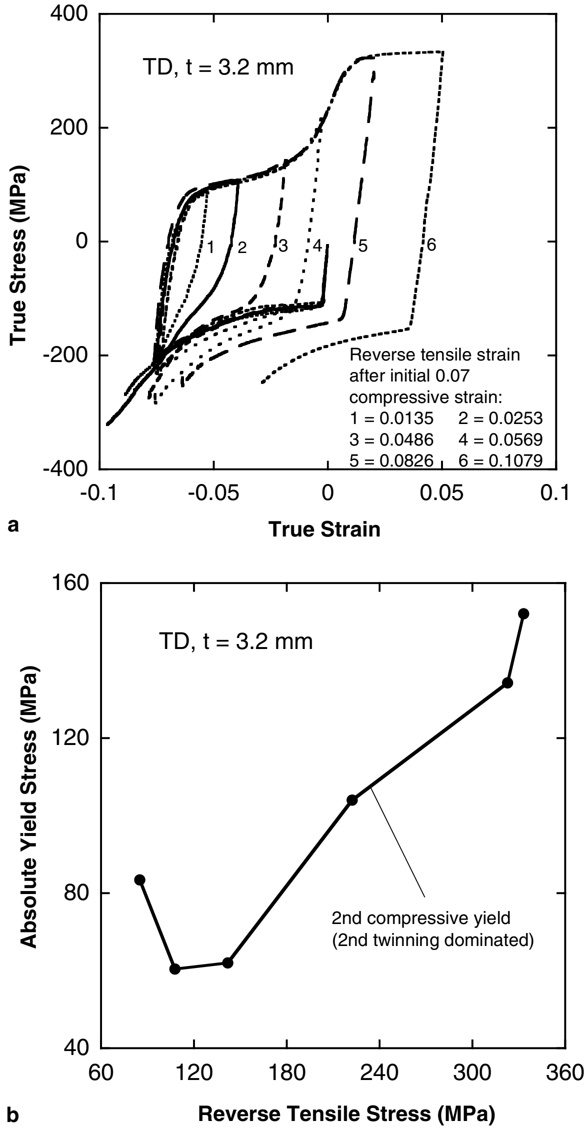

Fig. 23. Compression–tension-compression (C-T-C) results for various reverse tensile strains. (a) Raw stress–strain data; (b) variation of 2nd compressive yield stress (0.4% offset) with the final flow stress at the end of the tensile prestrain.

between the reverse tensile flow stress of 100 and 150 MPa, the second compressive yield stress remains constant. Comparison with Fig. 21c shows that the compressive yield following tension increases with pre-tensile stress. In one case the prestrain involves very limited twinning (~4%) whereas in the other there is nearly complete twinning and variable untwinning. The similarity of the results suggests that the compressive yield stress, determined mainly by twinning, is related to the accumulated slip activity, in the form of dislocation density.

5. Conclusions

A combination of mechanical and microstructural techniques has been used to reveal the nature and origin of continuous and reverse strain hardening of AZ31B magnesium sheet alloy. The techniques include large-strain, continuous tension/compression testing, simple shear deformation, acoustic emission technology, optical metallography, and X-ray texture measurement. The monotonic deformation behavior, consistent with the literature of Mg sheet deformation, involves multiple deformation mechanisms – basal slip, non-basal slip, and twinning. The reverse loading paths reveal new facets of the deformation behavior. The mechanistic interpretation of four strain paths are as follows:

1. For annealed sheet, uniaxial tensile deformation is dominated initially by basal slip with other contributions of non-basal slip and twinning to maintain local compatibility, giving way progressively to non-basal slip as the flow stress rises. This is consistent with reports in the literature (Agnew and Duygulu, 2005). The hardening curve for this stress state has the normal concave-down aspect.
2. In-plane compression of annealed sheet is initially predominantly by twinning with limited basal slip for compatibility, progressively becoming dominated by basal slip as the stress rises and twinning approaches exhaustion. The transitions among these two stages provide the unusual S-shaped hardening curve observed in compression. This interpretation is consistent with prior literature about deformation mechanisms of magnesium and magnesium alloy crystals (Kelly and Hosford, 1968).
3. In-plane tension following compressive deformation occurs predominantly by untwinning initially, a mechanism of shrinking existing twins that occurs at low applied stress relative to twinning because it does not require twin nucleation. Compatibility is maintained by slip. As existing twins disappear, the mechanism approaches exhaustion (the strain range depending on the degree of twinning introduced previously), and basal slip initially dominates, with growing fraction of non-basal slip. The transitions among the three predominant mechanisms produce an S-shaped hardening curve similar to that in compression of annealed material, initially at a lower stress because of the relative ease of untwinning, but eventually at higher stress because untwinning approaches exhaustion at a lower strain than that twinning did in compression.
4. In-plane simple shear excites a limited amount of twinning initially, consistent with observations of small thickness changes. (Such thickness changes also arise from imperfect boundary constraint of the shear specimen.) A concave-up hardening curve is observed, related to this twinning, with a similar shape upon reverse tension, consistent with untwinning.

Specific conclusions were also reached:

1. Acoustic emission (AE) signals of the burst type are strongly correlated with the nucleation of new twins, in agreement with a prior report (Toronchuk, 1977). The growth or shrinkage of twins, and deformation by slip, are more continuous and are nearly undetectable as AE burst activity. Therefore, strains from twinning cannot be correlated quantitatively to burst-type AE signals.

2. Direct evidence from multiple techniques shows that the early stages of tensile deformation following compression rely on untwinning rather than new twinning: a low flow stress consistent with no twin nucleation is observed, acoustic emission signals are low during tension but are high during compression, metallographic observations show that twin areal fractions decrease to prior levels during subsequent tension, and textures reverse to near-original ones upon subsequent tension. Texture reversal corresponding to a low reverse stress is consistent with a report in the literature (Kleiner and Uggowitzer, 2004).
3. The fraction of strain rate accommodated by twinning during compression has been estimated quantitatively. It is initially near 90% and drops to 50% at a strain of −0.05.
4. AE signals show a second range of intense twin nucleation at compressive strains of 0.06–0.07, near the exhaustion of primary twinning. Although it is has not been verified metallographically, this appearance presumably correlates with the activation of secondary twins of the type $\{10\bar{1}1\}$ and $\{30\bar{3}2\}$, as noted in the literature (Koike, 2005).
5. The exhaustion strain for 100% primary twinning (no slip contribution) is 0.059 for a perfectly c-textured, randomly a-textured, polycrystalline Mg sheet. A similar calculation shows that the r-value for pure primary twinning is −0.09.
6. In-plane plastic anisotropy, of both yield stress and plastic strain ratios, is greater in tension than in compression. The largest measured yield stresses and r-values are in the TD and the smallest in RD, consistent with texture predictions of the ease of non-basal slip (Agnew and Duygulu, 2003).
7. R-values evolve rapidly in tension, consistent with observations in the literature of progressively activated non-basal slip (Agnew and Duygulu, 2005).
8. Contrary to the behavior of ductile alloys with cubic crystal structures, fracture occurs in simple shear at equivalent strains less than those attainable in uniaxial tension. This appears to be related to higher constraint of simple shear and the difficulty of HCP alloys to meet the Von Mises condition for arbitrary deformation, thus promoting brittle fracture rather than plastic localization.
9. The magnitudes of three strengthening mechanisms related to twinning have been estimated using a novel analysis of cyclic hardening. For a strain range of 4%, the hardening contributions as obstacles to slip and the texture change attributable to twinning are approximately 9–10 MPa. The corresponding contribution of activation of twinning vs. untwinning is 17 MPa, approximately twice as large as the other contributions.

Acknowledgments

This work was sponsored through subcontract No. 4000028510 with UT-Battelle, with funding provided by the US Department of Energy, Assistant Secretary for Energy Efficiency and Renewable Energy, Office of FreedomCAR and Vehicle Technologies, as part of the High Strength Weight Reduction Materials Program. The authors thank Dr. Joe A. Horton (Oak Ridge National Laboratory) for providing the materials, Dr. Mark E. Walter (Ohio State University) for assistance with the acoustic emission technique, Dr. Frederic Barlat (Alcoa Technical Center) for the simple shear test equipment, and Dr. Carlos Tome (Los Alamos National Laboratories) for the VPSC code with twinning capabilities.

Appendix A. Equivalent in-plane compressive strain for a basal textured sheet with random in-plane orientation of $\langle a \rangle$ axes

Simple shear caused by deformation twinning is expressed in a local coordinate system as follows:

$$\boldsymbol{\varepsilon}' = \frac{1}{2}\begin{bmatrix} 0 & \gamma & 0 \\ \gamma & 0 & 0 \\ 0 & 0 & 0 \end{bmatrix} \tag{A1}$$

where γ depends on c/a ratio of HCP metals. For AZ31B alloy, $c/a = 1.624$ and $\gamma = 0.129$. Length change of arbitrary line element due to twinning can be examined by coordinate transformation as follows:

$$\boldsymbol{\varepsilon} = R\boldsymbol{\varepsilon}'R^{\mathrm{T}} \tag{A2}$$

where $\boldsymbol{\varepsilon}$ is strain tensor expressed in the arbitrary coordinate system; R is rotation matrix, the components of which, $R_{ij'}$, is the direction cosine between two axes i and j'.

Assuming an ideal basal texture with random in-plane $\langle a \rangle$ axes exists. Any arbitrary in-plane direction within $\pm 30°$ of each $\{0\,\bar{1}\,1\,2\}\langle 0\,1\,\bar{1}\,1\rangle$ twinning system is compressed with strain ε_{c} by its activation, where ε_{c} is obtained from Eq. (A2). Only 30° is considered due to crystalline symmetry. The effect of random in-plane $\langle a \rangle$ axes on equivalent compressive strain can be modeled by averaging ε_{c} of each line elements located between 0° and 30° away from the projection of twinning direction on basal plane as follows:

$$\bar{\varepsilon} = \frac{\int_{0°}^{30°} \varepsilon_c(\theta)\,\mathrm{d}\theta}{\int_{0°}^{30°} \mathrm{d}\theta} = -0.059 \tag{A3}$$

Equivalent r-value from twinning in in-plane compression can be examined as follows:

$$\bar{r} = \frac{\int_{0°}^{30°} r(\theta)\,\mathrm{d}\theta}{\int_{0°}^{30°} \mathrm{d}\theta} = -0.09 \tag{A4}$$

where r is defined by the ratio of plastic strain in transverse direction to that in thickness direction.

Appendix B. Texture softening during in-plane compression

The role of texture evolution on strain hardening can be assessed by texture analysis. Visco-Plastic Self-Consistent method (Lebensohn and Tome, 1993), embodied in the software package VPSC, is one such method. VPSC was used to simulate the tensile yield of two measured textures: (a) an initial texture as measured before deformation, Fig. 14a, and (b) a texture after compression to a strain of −0.07, Fig. 14c. The differences in the texture are predominantly related to twinning, rather than to slip because evolution of texture is nearly imperceptible over this small strain range.

For purposes of separating the role of texture evolution on the ease of slip, only slip modes were allowed in the tensile simulations: basal $\langle a \rangle$, prismatic $\langle a \rangle$ and pyramidal $\langle c + a$ slip modes were allowed while twinning modes were deactivated. A Voce-type hardening was employed

Table B1
Voce parameters for slip modes used in VPSC, in MPa

	τ_0^α	τ_1^α	θ_0^α
Basal $\langle a\rangle$	24	26	180
Prismatic $\langle a\rangle$	88	50	250
Pyramidal $\langle c+a\rangle$	160	80	100

$$\tau_{\mathrm{CRSS}}^\alpha = \tau_0^\alpha + \tau_1^\alpha\left[1 - \exp\left(\frac{-\theta_0^\alpha \gamma}{\tau_1^\alpha}\right)\right] \tag{B1}$$

where $\tau_{\mathrm{CRSS}}^\alpha$ denotes the threshold stress for slip system α; γ denotes accumulated shear strain in aggregate; τ_0^α, θ_0^α, θ_1^α are material parameters for slip system α. The constants were fit to reproduce the uniaxial tension flow curves along RD and TD as shown in Table B1.

Tension tests along RD starting from the two textures are simulated using parameters in Table B1. The 0.4% offset yield stresses computed for the annealed texture and the twinned (i.e. compressed to -0.07 strain) texture are 190 and 172 MPa, respectively. Therefore, twinning produces texture softening of 18 MPa when compressively straining from the annealed state (twin fraction = 0) to a strain of -0.07 (twin fraction = 0.72).

For application to a smaller strain range, the corresponding change of twin fraction (and therefore the corresponding texture) must be considered. For a strain range of 0.01–0.05, the corresponding twin fractions are 0.14–0.17 (average 0.155) and 0.57–0.58 (average 0.575), depending on whether the stage was tension or compression. The texture softening for this range can be estimated as follows:

$$\Delta\sigma_{\mathrm{texture}} = \frac{0.575 - 0.155}{0.72 - 0.0} \times (-18\ \mathrm{MPa}) \approx -10\ \mathrm{MPa} \tag{B2}$$

References

Abel, A., 1987. Historical perspectives and some of the main features of the Bauschinger Effect. Mater. Forum 10 (1), 11–26.

Agnew, S.R., 2002. Plastic anisotropy of magnesium alloy AZ31B sheet. In: Kaplan, H.I. (Ed.), TMS Annual Meeting, Magnesium Technology 2002. TMS, Seattle, Washington, USA, pp. 169–174.

Agnew, S.R., 2003. Private communication.

Agnew, S.R., 2005. Private communication.

Agnew, S.R., Duygulu, O., 2003. A mechanistic understanding of the formability of magnesium: examining the role of temperature on the deformation mechanisms. Mater. Sci. Forum 419–422, 177–188.

Agnew, S.R., Duygulu, O., 2005. Plastic anisotropy and the role of non-basal slip in magnesium alloy AZ31B. Int. J. Plast. 21, 1161–1193.

Agnew, S.R., Tome, C.N., Brown, D.W., Holden, T.M., Vogel, S.C., 2003. Study of slip mechanisms in a magnesium alloy by neutron diffraction and modeling. Scripta Mater. 48, 1003–1008.

Agnew, S.R., Yoo, M.H., Tome, C.N., 2001. Application of texture simulation to understanding mechanical behavior of Mg and solid solution alloys containing Li or Y. Acta Mater. 49, 4277–4289.

ASTM-E8-00, 2000. Standard test methods for tension testing of metallic materials. ASTM, West Conshohocken, PA, USA.

Atkinson, J.D., Brown, L.M., Stobbs, W.M., 1974. Work-hardening of Cu–silica. Pt. 4. Bauschinger Effect and plastic relaxation. Philos. Mag. 30 (6), 1247–1280.

Attari, N., Robin, C., Pluvinage, G. 1990. Cyclic plastic deformation by twinning of a magnesium alloy GA3Z1. In: (Ed.), Advanced Aluminium and Magnesium Alloys, Amsterdam, Netherlands, pp. 837–846.

Avery, D.H., Hosford, W.F., Backofen, W.A., 1965. Plastic anisotropy in magnesium alloy sheets. Trans. Metall. Soc. AIME 233, 71–78.

Bakarian, P.W., Mathewson, C.H., 1943. Slip and twinning of magnesium single crystals at elevated temperatures. Trans. AIME 152, 226.

Balakrishnan, V. 1999. Measurement of in-plane Bauschinger Effect in metal sheets. MS Thesis. The Ohio State University, Columbus, OH, USA.

Ball, E.A., Prangnell, P.B., 1994. Tensile-compressive yield asymmetries in high strength wrought magnesium alloys. Scripta Metall. Mater. 31 (2), 111–116.

Barnett, M.R., Keshavarz, Z., Beer, A.G., Atwell, D., 2004. Influence of grain size on the compressive deformation of wrought Mg–3Al–1Zn. Acta Mater. 52, 5093–5103.

Bauschinger, J. 1886. On the change of the elastic limit and the strength of iron and steel, by drawing out, by heating and cooling, and by repetition of loading (summary). Minutes of Proceedings of the Institution of Civil Engineers with Other Selected and Abstracted Papers LXXXVII, p. 463.

Bettles, C.J., Gibson, M.A., 2005. Current wrought magnesium alloys: strengths and weaknesses. JOM 57 (5), 46.

Boger, R.K., Wagoner, R.H., Barlat, F., Lee, M.G., Chung, K., 2005. Continuous, large strain, tension/compression testing of sheet material. Int. J. Plast. 21 (12), 2319–2343.

Bohlen, J., Chmelik, F., Dobron, P., Kaiser, F., Letzig, D., Lukac, P., Kainer, K.U., 2004a. Orientation effects on acoustic emission during tensile deformation of hot rolled magnesium alloy AZ31. J. Alloy. Compd. 378, 207–213.

Bohlen, J., Chmelik, F., Dobron, P., Letzig, D., Lukac, P., Kainer, K.U., 2004b. Acoustic emission during tensile testing of magesium AZ alloys. J. Alloy. Compd. 378, 214–219.

Bohlen, J., Chmelik, F., Kaiser, F., Letzig, D., Lukac, P., Kainer, K.U., 2002. Acoustic emission generated during tensile deformation of an AZ31 magnesium sheet. Kovove Mater. 40, 290–297.

Brown, D.W., Agnew, S.R., Bourke, M.A.M., Holden, T.M., Vogel, S.C., Tome, C.N., 2005. Internal strain and texture evolution during deformation twinning in magnesium. Mater. Sci. Eng. A 399, 1–12.

Brown, L.M., 1977. Orowan's explaination of the Bauschinger Effect. Scripta Metall. Mater. 11, 127–131.

Burke, E.C., Hibbard, W.R., 1952. Plastic deformation of magnesium single crystals. Trans. Metall. Soc. AIME 194, 295–303.

Caceres, C.H., Sumitomo, T., Veidt, M., 2003. Pseudoelastic behavior of cast magnesium AZ91 alloy under cyclic loading-unloading. Acta Mater. 51, 6211–6218.

Chmelik, F., Lukac, P., Janecek, M., Moll, F., Mordike, B.L., Kainer, K.U., Langdon, T.G., 2002a. An evaluation of the creep characteristics of an AZ91 magnesium alloy composite using acoustic emission. Mater. Sci. Eng. A 338, 1–7.

Chmelik, F., Ziegenbein, A., Neuhauser, H., Lukac, P., 2002b. Investigating the Portevin-Le Chatelier effect by the acoustic emission and laser extensometry techniques. Mater. Sci. Eng. A 324, 200–207.

Conrad, H., Robertson, W.D., 1957. Effect of temperature on the flow stress and strain-hardening coefficient of magnesium single crystals. Trans. AIME 209, 503.

Cubberly, W.H., Baker, H., Benjamin, D., Unterweiser, P.M., Kirkpatrick, C.W., Knoll, V., Nieman, K. (Eds.), . Properties and Selection: Nonferrous Alloys and Pure Metals, ninth ed.. Metals Handbook American Society for Metals.

Duygulu, O., Agnew, S.R., 2003. The effect of temperature and strain rate on the tensile properties of textured magnesium alloy AZ31B sheet. In: Kaplan, H. (Ed.), Magnesium Technology 2003. TMS, San Diego, CA, USA, pp. 237–242.

Friesel, M., Carpenter, S.H., 1984a. Determination of the source of acoustic emission generated during the deformation of magnesium. J. Acous. Emission 3 (1), 11–17.

Friesel, M.A., Carpenter, S.H., 1984b. An inverted strain rate dependence of the acoustic emission generated during the deformation of high purity a-Ti. Mater. Sci. Eng. 68, 107–111.

Gharghouri, M.A. 1997. PhD Thesis. McMaster University, Ont., Canada.

Gharghouri, M.A., Weatherly, G.C., Embury, J.D., Root, J., 1999. Study of the mechanical properties of Mg-7.7at.% Al by in-situ neutron diffraction. Philos. Mag. A 79 (7), 1671–1695.

Gsell, C., Boni, S., Shrivastava, S., 1983. Application of the plane simple shear test for determination of the plastic behavior of solid polymersat large strains. J. Mater. Sci. 18 (3), 903–918.

Hasegawa, T., Yakou, T., Kocks, U.F., 1986. Forward and reverse rearrangements of dislocations in tangled walls. Mater. Sci. Eng. 81 (1–2), 189–199.

Heiple, C.R., Carpenter, S.H., 1987. Acoustic emission produced by deformation of metals and alloys – a review: part I. J. Acous. Emission 6 (3), 177–207.

Horton, J.A., Blue, C.A., Muth, T., Bowles, A.L., Agnew, S.R., 2005a. Infrared processing of magnesium wrought alloys. In: Neelameggham, N.R., Kaplan, H.I., Powell, B.R. (Eds.), Magnesium Technology 2005. TMS, San Francisco, CA, USA, pp. 155–158.

Horton, J.A., Agnew, S.R., Diamond, S., Sklad, P.S., 2005b. Wrought magnesium alloy/process development. In: Wall, E., Sullivan, R., Diamond, S. (Eds.), FY 2004 Process Report for High Strength Weight Reduction Materials. US Department of Energy, Washington, DC, pp. 25–32.

Hsu, S.S., Cullity, B.D., 1954. On the torsional deformation and recovery of single crystals. Trans. AIME 200, 305.

Huang, M., Jiang, L., Liaw, P.K., Brooks, C.R., Seeley, R., Klarstrom, D.L., 1998. Using acoustic emission in fatigue and fracture materials research. JOM-e 50 (11).

Jain, A., Agnew, S.R., 2006. Modeling the temperature dependent effect of twinning on the behavior of magnesium alloy AZ31B sheet. Mater. Sci. Eng. A, in press.

Kang, G., Ohno, N., Nebu, A., 2003. Constitutive modeling of strain range dependent cyclic hardening. Int. J. Plast. 19, 1801–1819.

Kallend, J.S., Kocks, U.F., Rollet, A.D., Wenk, H.R., 1991. Operational texture analysis. Mater. Sci. Eng. A 132, 1–11.

Karaman, I., Sehitoglu, H., Chumlyakov, Y.I., Maier, H.J., Kireeva, I.V., 2001. The effect of twinning and slip on the Bauschinger Effect of Hadfield steel single crystals. Metall. Mater. Trans. A 32A, 695–706.

Kelly, E.W., Hosford, W.F., 1968. Plane-strain compression of magnesium and magnesium alloy crystals. Trans. Metall. Soc. AIME 242, 5–13.

Keshavarz, Z., Barnett, M.R., 2005. In-situ investigation of twinning behavior in Mg–3Al–1Zn. In: Neelameggham, N.R., Kaplan, H.I., Powell, B.R. (Eds.), Magnesium Technology 2005. TMS, San Francisco, CA, USA, pp. 171–175.

Kleiner, S., Uggowitzer, P.J., 2004. Mechanical anisotropy of extruded Mg–6% Al–1% Zn alloy. Mater. Sci. Eng. A 379, 258–263.

Klimanek, P., Potzsch, A., 2002. Microstructure evolution under compressive plastic deformation of magnesium at different temperatures and strain rates. Mater. Sci. Eng. A 324, 145–150.

Kocks, U.F., Westlake, D.G., 1967. The important of twinning for the ductility of CPH polycrystals. Trans. Metall. Soc. AIME 239, 1107–1109.

Koike, J., 2005. Enhanced deformation mechanisms by anisotropic plasticity in polycrystalline Mg alloys at room temperature. Metall. Mater. Trans. A 36A (7), 1689–1696.

Koike, J., Kobayashi, T., et al., 2003. The activity of non-basal slip systems and dynamic recovery at room temperature in fine-grained AZ31B magnesium alloys. Acta Mater. 51, 2055–2065.

Koike, J., Ohyama, R., 2005. Geometrical criterion for the activation of prismatic slip in AZ61 Mg alloy sheets deformed at room temperature. Acta Mater. 53 (7), 1963–1972.

Lamark, T.T., Chmelik, F., Estrin, Y., Lukac, P., 2004. Cyclic deformation of a magnesium alloy investigated by the acoustic emission technique. J. Alloy. Compd. 378, 202–206.

Lebensohn, R.A., Tome, C.N., 1993. A self-consistent anisotropic approach for the simulation of plastic deformation and texture development in polycrystals-application to zirconium alloys. Acta Metall. 41, 2611–2624.

Liu, Y., Xie, Z., Humbeeck, J.V., Delaey, L., 1999. Some results on the detwinning process in NiTi shape memory alloys. Scripta Mater. 41 (12), 1273–1281.

Liu, Y., Xie, Z.L., 2003. Twinning and detwinning of $\langle 0\,1\,1\rangle$ type II twin in shape memory alloy. Acta Mater. 51, 5529–5543.

Lopes, A.B., Barlat, F., Gracio, J.J., Duarte, J.F.F., Rauch, E.F., 2003. Effect of texture and microstructure on strain hardening anisotropy for aluminum deformed in uniaxial tension and simple shear. Int. J. Plast. 19 (1), 1–22.

Margolin, H., Hazaveh, F., Yaguchi, H., 1978. The grain boundary contribution to the Bauschinger Effect. Scripta Metall. Mater. 12 (12), 1141–1145.

McDonald, J.C., 1937. Grain orientation in rolled magnesium alloys. Phys. Rev. 52, 886–887.

Magnesium Elektron Wrought Products North America, 1001 College Street, P.O. Box 258, Madison, IL 62060, USA.

MetalMart International, Inc. Mark Metals Division, 12225 Coast DR., Whittier, CA 90601, USA.

Miura, S., 2004. Unpublished research. Hokkaido University, Hokkaido, Japan.

Nave, M.D., Barnett, M.R., 2004. Microstructures and textures of pure magnesium deformed in plane-strain compression. Scripta Mater. 51 (881–885).

Nobre, J.P., Noster, U., Kommeier, M., Dias, A.M., Scholtes, B., 2002. Deformation asymmetry of AZ31 wrought magnesium alloy. Key Eng. Mater. 230–232, 267–270.
Noster, U., Scholtes, B., 2003. Isothermal strain-controlled quasi-static and cyclic deformation behavior of magnesium wrought alloy AZ31. Z. Metallkd. 94 (5), 559–563.
Obara, T., Yoshinga, H., Morozumi, S., 1973. $\{11\overline{2}\overline{2}\}\langle\bar{1}\,\overline{1}\,\overline{2}\,\overline{3}\rangle$ slip system in magnesium. Acta Metall. Mater. 21, 845–853.
Ohno, N., 1982. A constitutive model of cyclic plasticity with a nonhardening strain region. J. Appl. Mech. 49, 721–727.
Partridge, P.G., 1965. Cyclic twinning in fatigued close-packed hexagonal metals. Philos. Mag. 12, 1043–1054.
Partridge, P.G., 1967. The crystallography and deformation modes of hexagonal close-packed metals. Metall. Rev. 12, 169–194.
Perez-Prado, M.T., Ruano, O.A., 2002. Texture evolution during annealing of magnesium AZ31 alloy. Scripta Mater. 46, 149–155.
Rauch, E.F., 1998. Plastic anisotropy of sheet metals by simple shear tests. Mater. Sci. Eng. A 241, 179–183.
Rauch, E.F., Schmitt, J.H., 1989. Dislocation substructures in mild steel deformed in simple shear. Mater. Sci. Eng. A 113, 441–448.
Reed, J.M., Walter, M.E., 2003. Observation of serrated flow of an Al–Mg alloy. Mater. Sci. Eng. A 359, 1–10.
Reed-Hill, R.E., 1973. Role of deformation twinning in determining the mechanical properties of metalsThe Inhomogeneity of Plastic Deformation. American Society for Metals, pp. 285–311.
Reed-Hill, R.E., Abbaschian, R., 1994. Physical Metallurgy Principles. PWS Publ. Company, Boston.
Reed-Hill, R.E., Robertson, W.D., 1957a. Additional modes of deformation twinning in magnesium. Acta Metall. 5, 717–727.
Reed-Hill, R.E., Robertson, W.D., 1957b. Deformation of magnesium single crystals by nonbasal slip. Trans. TMS-AIME 220, 496–502.
Roberts, C.S., 1960. Magnesium and Its Alloys. Wiley, New York/London.
Schmid, E., 1931. Beitrage zur Physik und Metallographie des Magnesiums. Z. Elektrochem. 37, 447.
Sehitoglu, H., Hamilton, R., Canadinc, D., Zhang, X.Y., Gall, K., Karaman, I., Chumlyakov, Y., Maier, H.J., 2003. Detwinning in NiTi alloys. Metall. Mater. Trans. A 34A, 5–13.
Skalskyi, V.R., Andreikiv, O.E., Serhienko, O.M., 2003. Investigation of the plastic deformation of materials by the acoustic emission method (review). Mater. Sci. 39 (1), 86–107.
Staroselsky, A., Anand, L., 2003. A constitutive model for hcp materials deforming by slip and twinning: application to magnesium alloy AZ31B. Int. J. Plast. 19, 1843–1864.
Styczynski, A., Hartig, C., Bohlen, J., Letzig, D., 2004. Cold rolling textures in AZ31 wrought magnesium alloy. Scripta Mater. 50, 943–947.
Taylor, G.I., 1938. Plastic strain in metals. J. Inst. Met. 62, 307.
Toronchuk, J.P., 1977. Acoustic emission during twinning of zinc single crystals. Mater. Eval. (October), 51–53.
Von Mises, R., 1928. Mechanik der plastischen formanderung von kristallen. Z. Angew. Math. Mech. 8, 161–185.
Wagoner, R.H., Chenot, J.L., 1996. Fundamentals of Metal Forming. Wiley, New York.
Ward Flynn, P., Mote, J., Dorn, J.E., 1961. On the thermally activated mechanism of prismatic slip in magnesium single crystals. Trans. TMS-AIME 221, 1148–1154.
Yoo, M.H., 1981. Slip, twinning, and fracture in hexagonal close-packed metals. Metall. Mater. Trans. A 12A, 409–418.
Yoo, M.H., Morris, J.R., Ho, K.M., Agnew, S.R., 2002. Nonbasal deformation modes of HCP metals and alloys: role of dislocation source and mobility. Metall. Mater. Trans. A 33, 813.
Yukutake, E., Kaneko, J., Sugamata, M., 2003. Anisotropy and non-uniformity in plastic behavior of AZ31 Magnesium alloy plates. Mater. Trans. 44 (4), 452–457.